JM PAPERS

On the laminar solutions and stability of accelerating and decelerating channel flows

Alec J. Linot[1,†], **Peter J. Schmid**[2] **and Kunihiko Taira**[1]

[1]Department of Mechanical and Aerospace Engineering, University of California, Los Angeles, CA 90095, USA

[2]Department of Mechanical Engineering, Division of Physical Sciences and Engineering (PSE), King Abdullah University of Science and Technology (KAUST), Thuwal, Saudi Arabia

We study the effect of acceleration and deceleration on the stability of channel flows. To do so, we derive an exact solution for laminar profiles of channel flows with an arbitrary, time-varying wall motion and pressure gradient. This solution then allows us to investigate the stability of any unsteady channel flow. In particular, we restrict our investigation to the non-normal growth of perturbations about time-varying base flows with exponentially decaying acceleration and deceleration, with comparisons to growth about a constant base flow (i.e. the time-invariant simple shear or parabolic profile). We apply this acceleration and deceleration through the velocity of the walls and through the flow rate. For accelerating base flows, perturbations never grow larger than perturbations about a constant base flow, while decelerating flows show massive amplification of perturbations – at a Reynolds number of 500, properly timed perturbations about the decelerating base flow grow $O(10^5)$ times larger than perturbations grow about a constant base flow. This amplification increases as we raise the rate of deceleration and the Reynolds number. We find that this amplification arises due to a transition from spanwise perturbations leading to the largest amplification to streamwise perturbations leading to the largest amplification that only occurs in the decelerating base flow. By evolving the optimal perturbations through the linearized equations of motion, we reveal that the decelerating base flow achieves this massive amplification through the Orr mechanism, or the down-gradient Reynolds stress mechanism, which accelerating and constant base flows cannot maintain.

Key words: Navier-Stokes equations, shear-flow instability

† Email address for correspondence: aleclinot@gmail.com

A.J. Linot, P.J. Schmid and K. Taira

1. Introduction

In the study of flow stability a frequently overlooked topic is the stability of unsteady, aperiodic flows. Despite this oversight, these transient flows appear in many systems like airfoil gust encounters (Jones 2020), start-up flow in a pipe (Kataoka, Kawabata & Miki 1975) and particle sedimentation (Guazzelli & Hinch 2011). A common feature of unsteady flows is that under acceleration, the flow tends to stabilize, while under deceleration, the flow tends to destabilize. Such trends have been observed and analysed for both periodic flows (Gerrard 1971; Hino *et al.* 1983) and transient flows (Kurokawa & Morikawa 1986; Shuy 1996; He & Jackson 2000). Understanding the mechanism by which this stabilization or destabilization occurs is highly valuable as it could either be used as a tool to actuate steady flows or it could be used to inform control of already unsteady flows. Two key challenges with systematically investigating the stability of unsteady laminar flows are: (1) the base profile about which to perform the analysis may be unknown, and (2) standard linear stability methods examine the long-time dynamics of a time-invariant linear operator, while for unsteady flows we wish to examine transient dynamics associated with a time-varying linear operator.

Although analytical laminar profiles are known for various boundary conditions (Drazin & Riley 2006), solutions are not known for arbitrary boundary conditions. Two widely studied geometries with many different analytical laminar solutions are pipe flow and channel flow. The different analytical solutions for pipe flow correspond to different pressure gradients (these pressure gradients may be dictated by a prescribed flow rate), and the different analytical solutions for channel flows correspond to different pressure gradients and wall motion. The simplest cases are either constant pressure gradient or constant, opposite wall motion (in the channel flow case). The former results in a parabolic flow (Poiseuille) and the latter in simple shear flow (Couette) (Bird *et al.* 2015).

Unlike the constant pressure gradient case, an unsteady pressure gradient yields different solutions between the pipe and channel geometries. First, we discuss some of the unsteady solutions in pipe flow. A widely studied flow type is pulsatile or Womersley flow (Womersley 1955). This flow corresponds to pipe flow driven by a periodic pressure gradient. Although Womersley's derivation is widely cited, earlier derivations of this profile exist (Szymanski 1932), as noted in Urbanowicz *et al.* (2023). Other common solutions for pipe flow are start-up flow by either a discontinuous change in the pressure gradient (Szymanski 1932) or a linear ramp change in the pressure gradient (Ito 1952). Kannaiyan, Varathalingarajah & Natarajan (2021) later extended these start-up solutions for prescribing the flow rates instead of pressure gradients. Fan (1964) also found solutions for general pressure gradients and for rectangular ducts. For a more complete review of solutions in pipe flow, we refer the reader to Urbanowicz *et al.* (2023).

Next, we survey analytical solutions for channel flows. Two classical solutions in this domain are Stokes' first and second problems (Batchelor 2000; Liu 2008; Schlichting & Gersten 2017). These solutions correspond to the cases of instantaneously moving a wall from rest and periodic wall motion. In addition to these solutions, there also exists a solution for a periodic pressure gradient in channel flows (Majdalani 2008) – this differs from Womersley flow in a pipe. Majdalani (2008) also provided solutions for arbitrary periodic pressure gradients. This work was extended by Lee (2017) to include pressure gradients that are not periodic in both pipes and channel flow, for motionless initial conditions. Finally, Daidzic (2022) derived an analytical solution for arbitrary periodic pressure gradients or wall motion. We emphasize that the analytical solutions presented in this work are for arbitrary wall motion and pressure gradients (not necessarily periodic) and for arbitrary initial conditions. Furthermore, we will show how to compute the

pressure gradient for a prescribed flow rate. This is an important extension for investigating accelerating and decelerating pressure-driven flow (PDF).

Once a laminar flow profile is known, the next challenge consists of performing stability analysis about this profile. When the laminar profile exhibits periodic time-varying dynamics, traditional methods of linear stability analysis about a fixed point can be extended with Floquet analysis (Davis 1976). von Kerczek & Davis (1974) applied Floquet analysis to Stokes' second problem and found that the flow was even more stable than a motionless fluid. Later, von Kerczek (1982) applied Floquet analysis to pulsatile channel flow and again showed that the motion had a stabilizing effect, and Tozzi & von Kerczek (1986) later performed Floquet analysis for pulsatile pipe flow. More recently, Pier & Schmid (2017) provided a comprehensive Floquet analysis of pulsatile channel flow in which they found destabilization of the flow at low frequencies. In this linearly unstable regime, they found a 'cruising' regime where nonlinearity is sustained over a period and a 'ballistic' regime where trajectories exhibit large growth to a nonlinear phase before returning to small amplitudes within a cycle.

While Floquet analysis is appropriate for periodic flows it does not apply to aperiodic flows. One approach to investigating the stability of time-varying flows is to consider the stability of the instantaneous profile as if it were 'frozen' (i.e. the quasi-steady state approximation). For example, linear stability analysis has been performed using this quasi-steady state approximation in start-up pipe flow (Kannaiyan, Natarajan & Vinoth 2022). However, this approach breaks down when the laminar profile changes faster than perturbations grow or decay in the linear stability analysis, and the linear stability analysis does not provide this time scale. Shen (1961) discusses further challenges with this approach.

An alternative to linear stability analysis is the energy method (Serrin 1959; Joseph 1976). Whereas linear stability indicates long-time growth, the energy method reveals when a perturbation will lead to immediate growth in energy E (i.e. this method finds perturbations where $dE/dt > 0$ at the instant the perturbation is applied). To apply this method to unsteady base flows, the quasi-steady state approximation must again be taken. Because this method quantifies the instantaneous behaviour, the assumption is less detrimental than the frozen stability analysis, which reveals the asymptotic stability. Additionally, an advantage of this method is that it can be formulated in terms of the relative energy of the perturbation in relationship to the base flow (Shen 1961). Conrad & Criminale (1965) applied this method to accelerating and decelerating channel profiles with wall boundary conditions of $1 - e^{-\kappa t}$ and $e^{-\kappa t}$ (among other profiles). Their results showed that acceleration increased the critical Reynolds number, while deceleration decreased it. However, we note that the energy method dramatically underestimates the critical Reynolds number at which flows go through transition. Moreover, it does not provide the shape of the perturbation or the amount of growth that perturbations exhibit.

We overcome these problems associated with both linear stability analysis and the energy method by instead investigating stability using optimal perturbation theory of the time-varying linearized equations. In this method, we find the perturbation energy growth over a finite time window (Schmid & Henningson 2001). This differs from the energy method in that it restricts the perturbations to physically realizable fields, it does not account for nonlinearity and it amounts to the growth over a finite window. The optimal perturbation method captures the effects of non-normal growth missed by linear methods (Trefethen *et al.* 1993). Butler & Farrell (1992) computed the optimal perturbations for constant wall motion in a channel flow and found that pairs of streamwise vortices produce the largest growth. Reddy & Henningson (1993) also found the optimal perturbations

for constant wall motion and for a constant pressure gradient in channel flows. They again showed that the largest growing perturbations only vary in the spanwise direction. Similarly, Schmid & Henningson (1994) found that azimuthal-dependent perturbations lead to the largest growth when computing the optimal perturbations for constant pressure gradient pipe flow. In both Reddy & Henningson (1993) and Schmid & Henningson (1994), the energy growth was shown to scale as the Reynolds number squared.

Optimal perturbations have also been determined for some unsteady flows. Biau (2016) computed the optimal perturbations for Stokes' second problem and found that streamwise perturbations resulted in the largest growth, which scales exponentially with the Reynolds number. Xu, Song & Avila (2021) investigated growth in pulsatile pipe flows and found that, at certain Womersley numbers and amplitudes, helical perturbations dominated with an exponential scaling at high Reynolds numbers and quadratic scaling at low Reynolds numbers. Finally, one of the few studies of an unsteady, aperiodic flow was performed by Nayak & Das (2017). They computed the optimal perturbation for channel flow impulsively stopped from a constant pressure gradient. The optimal perturbations in this case are again streamwise structures. Our investigation of accelerating and decelerating flows will link together the differences in *Re* scaling observed between the constant and unsteady flows described here.

In the present work, we investigate the transient growth of perturbations in unsteady channel flows that exhibit exponentially decaying acceleration and deceleration. Section 2 derives the analytical solutions for arbitrary wall motion (§ 2.1) and pressure gradients (§ 2.2) for channel flows. In § 3 we investigate the transient growth of perturbations to laminar solutions associated with acceleration and deceleration of the wall velocity and flow rate. Section 3.1 presents the approach taken to compute this transient growth through the linearized equations of motion and examples of this growth at a specific wavenumber. Following this, in § 3.2 we compute the maximum growth as we vary Reynolds numbers and acceleration or deceleration. Notably, as we increase deceleration, perturbations become far more amplified, and the most amplified perturbations shift from spanwise structures to streamwise structures. Acceleration shows less amplification and the most amplified perturbations maintain a spanwise structure. In § 3.3 we study the evolution of these perturbations and find that energy in the decelerating case grows via the Orr mechanism at high Reynolds number and deceleration rates. We then validate the growth of these perturbations in direct numerical simulations (DNS) in § 3.4. We find the optimal timing of these perturbations in § 3.5. Finally, in § 4 we summarize our results and discuss future prospects.

2. Exact solutions for time-varying wall-driven and pressure-driven channel flow

We first need to determine the underlying laminar flow solutions to investigate the stability of unsteady laminar flows. Figure 1 illustrates the configuration of interest – an incompressible fluid confined between two plates moving with arbitrary speed in opposite directions and with an arbitrary pressure gradient.

We seek laminar profiles in this domain that satisfy the incompressible Navier–Stokes equations (NSEs)

$$\frac{\partial \boldsymbol{u}}{\partial t} + \boldsymbol{u} \cdot \nabla \boldsymbol{u} = -\nabla p + \frac{1}{Re}\nabla^2 \boldsymbol{u}, \quad \nabla \cdot \boldsymbol{u} = 0, \tag{2.1}$$

which have been non-dimensionalized by some characteristic velocity U_b, the channel half-height h and the kinematic viscosity ν, defining the Reynolds number as $Re = U_b h/\nu$. For an arbitrary wall motion and pressure gradient, the characteristic velocity U_b varies,
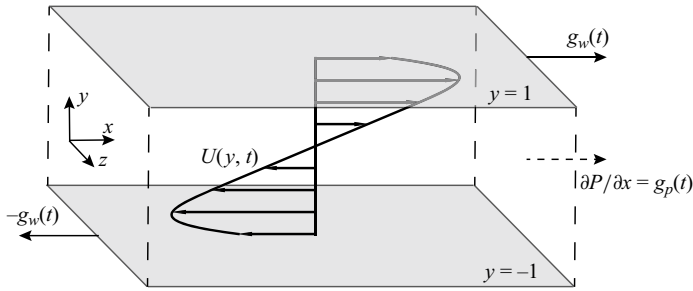
Figure 1. Diagram of a mixed wall and pressure-driven channel flow, with an example snapshot of the laminar flow for exponentially decaying wall motion.

and we will mention natural choices for specific examples. In (2.1) we define spatial coordinates in the streamwise $x \in [-\infty, \infty]$, wall-normal $y \in [-1, 1]$ and spanwise $z \in [-\infty, \infty]$ directions with the velocity vector $\boldsymbol{u} = [u, v, w]$ and pressure p.

For finding laminar solutions to (2.1), we restrict our search to streamwise velocity profiles that only depend on the wall-normal location and time $U(y, t)$. Inserting functions of this form into (2.1) yields

$$\frac{\partial U}{\partial t} = -g_p(t) + \frac{1}{Re}\frac{\partial^2 U}{\partial y^2}, \qquad (2.2)$$

where $g_p(t)$ is the pressure gradient. Here, we prescribe boundary conditions

$$U(y = \pm 1, t) = \pm g_w(t) + g_e(t). \qquad (2.3)$$

It is important to prescribe the boundary conditions as in (2.3), as it allows for arbitrary top and bottom wall motion. Furthermore, this formulation allows us to seek even and odd solutions to satisfy these boundary conditions. We also prescribe the initial condition

$$U(y, t = 0) = h_o(y) + h_e(y), \qquad (2.4)$$

where function $h_o(y)$ is an odd function with boundary conditions $h_o(\pm 1) = \pm g_w(0)$ and the function $h_e(y)$ is an even function with boundary conditions $h_e(\pm 1) = g_e(0)$. The superposition of these terms allows for all possible y-dependent initial conditions. For example, if we wish to start from uniform shear then $h_o(y) = y$ and $h_e(y) = 0$, or if we want to start with a parabolic profile then $h_o(y) = 0$ and $h_e(y) = 1 - y^2$. Detailed reasons for this split in symmetries will be presented in §§ 2.1 and 2.2.

Equation (2.2) is simply a heat equation with a forcing due to the pressure gradient $g_p(t)$. The linear nature of this equation allows us to add solutions together via linear superposition (Deen 2012). Thus, solving this equation requires adding solutions together in order to recast the problem into a canonical form we can subsequently solve with a sum over basis functions, e.g. Fourier modes. Specifically, this involves adding solutions such that the resulting partial differential equation can be exactly reconstructed by our choice of basis functions. To this end, we first find a solution for odd wall motion ($g_w \neq 0$, $g_e = 0$, $g_p = 0$), after which we seek a solution for arbitrary pressure gradients and even wall motion ($g_w = 0$, $g_e \neq 0$, $g_p \neq 0$). These solutions can be summed to drive the flow with both wall motion and a pressure gradient. We will refer to odd wall motion cases as wall-driven flow (WDF) and to pressure gradient cases as PDF.

Finally, although we only consider streamwise wall motion, this formulation is valid for arbitrary streamwise and spanwise wall motion. This is straightforward to show if we

consider laminar solutions $\boldsymbol{u} = [U(y,t), 0, W(y,t)]$. Inserting this solution into (2.1), we obtain (2.2) and

$$\frac{\partial W}{\partial t} = -g_{p,z}(t) + \frac{1}{Re}\frac{\partial^2 W}{\partial y^2},\tag{2.5}$$

where $g_{p,z}(t)$ denotes the pressure gradient in the spanwise direction. The boundary conditions and initial condition would match those above (except in the spanwise direction), thus, the solution we present in the streamwise direction is also valid in the spanwise direction. Combining these two solutions then allows us to find the laminar solution for arbitrary in-plane wall motion and pressure gradients.

2.1. *Wall-driven flow*

In the case of time-varying WDF, we seek odd functions $U(y,t) = -U(-y,t)$, which is a natural choice because the boundary conditions satisfy this behaviour. In Cartesian coordinates, this implies that we solve the heat equation using a sine basis. We achieve this by seeking solutions of the form

$$U(y,t) = f_w(y,t) + \frac{Re}{6}\frac{dg_w}{dt}(y^3 - y) + g_w(t)y.\tag{2.6}$$

Inserting this expression into (2.2)–(2.4) results in an equation for f_w,

$$\frac{\partial f_w}{\partial t} + \frac{Re}{6}\frac{d^2 g_w}{dt^2}(y^3 - y) = \frac{1}{Re}\frac{\partial^2 f_w}{\partial y^2},\tag{2.7}$$

with boundary conditions

$$f_w(y = \pm 1, t) = 0\tag{2.8}$$

and initial condition

$$f_w(y, 0) = h_o - \frac{Re}{6}\left.\frac{dg_w}{dt}\right|_{t=0}(y^3 - y) - g_w(0)y.\tag{2.9}$$

Through this linear superposition of solutions, f_w is now in a suitable form to be represented as

$$f_w(y, t) = \sum_{n=1}^{\infty}\hat{f}_{w,n}(t)\sin(n\pi y).\tag{2.10}$$

Notably, by including the additional terms in (2.6) both the boundary condition for f_w, the initial condition for f_w and all terms in (2.7) go to zero at the boundary, just like the sine basis. Had we omitted $(Re/6)(dg_w/dt)(y^3 - y)$ in (2.6), (2.7) would contain y, which has different boundary conditions at $y = 1$ and $y = -1$. Thus, if we were to recreate y with a periodic function there would be a discontinuity at the boundary, resulting in Gibbs phenomena (Graham & Rawlings 2013). In Appendix A we elaborate on this alternative approach and show that the error is larger than using (2.6).

999 A43-6

Next, we find the coefficients $\hat{f}_{w,n}(t)$ of the sine expansion. By combining (2.10) with (2.7) and taking the inner product with $\sin(m\pi y)$, we obtain

$$\frac{d\hat{f}_{w,m}}{dt} = -\frac{2Re(-1)^m}{(\pi m)^3}\frac{d^2 g_w}{dt^2} - a_m \hat{f}_{w,m}, \tag{2.11}$$

where $a_m = (\pi m)^2/Re$. Solving for this equation, we arrive at

$$\hat{f}_{w,m} = e^{-a_m t}\left(-\frac{2Re(-1)^m}{(\pi m)^3}\int_0^t e^{a_m t'}\left.\frac{d^2 g_w}{dt^2}\right|_{t=t'}dt' + C_{1,m}\right), \tag{2.12}$$

where $C_{1,m}$ can be determined by taking the inner product of the initial condition ((2.9)) with $\sin(m\pi y)$,

$$C_{1,m} = -\frac{2Re(-1)^m}{(\pi m)^3}\left.\frac{dg_w}{dt}\right|_{t=0} + \int_{-1}^{1}(h_o - g_w(0)y)\sin(m\pi y)\,dy. \tag{2.13}$$

If the initial condition is the simple shear profile and $g_w(0) = 1$, then $C_{1,m} = 0$. Finally, substituting $\hat{f}_{w,n}$ into (2.6), we find the laminar flow solution

$$U(y,t) = \sum_{n=1}^{\infty} e^{-a_n t}\left[-\frac{2Re(-1)^n}{(\pi n)^3}\left(\int_0^t e^{a_n t'}\left.\frac{d^2 g_w}{dt^2}\right|_{t=t'}dt' + \left.\frac{dg_w}{dt}\right|_{t=0}\right) + C_{1,n}\right]\sin(n\pi y)$$
$$+ \frac{Re}{6}\frac{dg_w}{dt}(y^3 - y) + g_w(t)y. \tag{2.14}$$

For many $g_w(t)$ profiles of interest, the integral in (2.14) may be evaluated directly. In Appendix A we provide some specific profiles of interest (see table 1 in Appendix A) and we validate the solution against other known laminar solutions. Here, we intend to study the effect of acceleration and deceleration on stability characteristics. Hence, the two profiles we concentrate on are exponentially decaying acceleration and deceleration from simple shear. These profiles are given by

$$g_w(t) = 1 - e^{-\kappa t} \tag{2.15}$$

for acceleration and

$$g_w(t) = e^{-\kappa t} \tag{2.16}$$

for deceleration. In both cases, we set the characteristic velocity for the Reynolds number as the maximum wall velocity over an infinite time horizon. We further discuss the nuances of this choice of non-dimensionalization in § 2.3.

The analytical laminar solution derived here, in combination with the derivation in the subsequent section enables us to consider arbitrary in-plane wall motion and pressure gradients. Thus, the approach we take with the prescribed exponentially decaying acceleration and deceleration can be applied to any in-plane flow, opening the possibility of investigating a wide range of unsteady flows. In particular, we hope this approach will inspire further investigation into aperiodic flows, which have largely been ignored compared with periodic flows. We choose to focus on the exponentially decaying acceleration and deceleration since it is one of the simplest forms of acceleration and deceleration that is bounded. Had we constantly accelerated or decelerated the wall, the flow would grow unbounded. Furthermore, constant deceleration would eventually turn into acceleration in the opposite direction.

This form of acceleration and deceleration is also of practical interest. This type of flow can be experienced in the start-up and shutdown of internal flows, including pipe flow (Greenblatt & Moss 2004) and flow around moving bodies, such as accelerating and decelerating airfoils (Sengupta *et al.* 2007). Also, unsteady separation bubbles can impose rapid acceleration or deceleration on the flow near the body, for example, during dynamic stall. McCroskey (1981) directly compares the vortex structures of an impulsively started plate to vortex structures during dynamic stall. Furthermore, exponentially decaying acceleration and deceleration are relevant problems when a controller is used to target a set point. If the system is first order then exponential decay occurs when we apply a step change to the system (Seborg *et al.* 2010). Additionally, exponentially decaying acceleration and deceleration are a reasonable proxy for the type of profile exhibited by an overdamped proportional-integral-derivative controller.

Use of an analytical solution, as opposed to a numerical simulation, also offers many advantages. First, our analytical solution depends upon both Re and κ, so we would have to perform a numerical simulation any time we changed these parameters. This would be far slower than evaluating the analytical solution, especially if we considered a flow with even more non-dimensional parameters. Second, at sufficiently high Reynolds numbers the numerical simulations could become unstable and trigger turbulence due to transient growth prevalent in these flows, which we will further discuss in § 3. Third, even if the solution does not diverge, numerical errors will accumulate in time, while we would not see these errors in our analytical laminar solution (instead, errors in the analytical solution will stem from truncating the summation). This last point is especially important since the stability analysis requires both first and second derivative information on the laminar profile. Finally, just knowing the form of the analytical solution is useful. For example, we can use (2.14) to prescribe wall motion that achieves desired laminar profiles. Perhaps, this fact could be utilized to achieve the fastest transition between flow profiles or to find a transition that minimizes the transient growth of perturbations. Regardless, knowledge of the analytical solution can be a powerful tool in understanding and controlling flows.

Figure 2 shows the accelerating laminar profiles at $Re = \{10, 500\}$ and $\kappa = \{0.01, 0.1\}$. Similarly, figure 3 shows the deceleration laminar profiles for the same parameters. At low Reynolds numbers Re and low values of κ the flow closely resembles simple shear at different shear rates (i.e. $U = g_w(t)y$), whereas with increased Re and κ the profiles become more curved. This curvature stems from a delay in the transfer of momentum from the wall to the middle of the channel. At higher Re this transfer is slower and at higher κ the rate of change of velocity at the wall increases. At the largest values of Re and κ the difference between acceleration and deceleration is exemplified. In this case, we observe that the accelerating profile maintains a positive gradient throughout the domain, while the decelerating profile shows a negative gradient near the wall. In § 3 we investigate the influence of these profiles on the stability of the flow.

2.2. *Pressure-driven flow*

We follow a similar approach to find the laminar flow solution for time-varying pressure gradients. In the case of PDF, we expect the solution to be even $U(y, t) = U(-y, t)$. In Cartesian coordinates, this suggests a solution of the heat equation using a cosine basis. We thus seek solutions of the form

$$U(y, t) = f_p(y, t) + \frac{Re}{2}g_p(t)(y^2 - 1) + g_e(t). \tag{2.17}$$
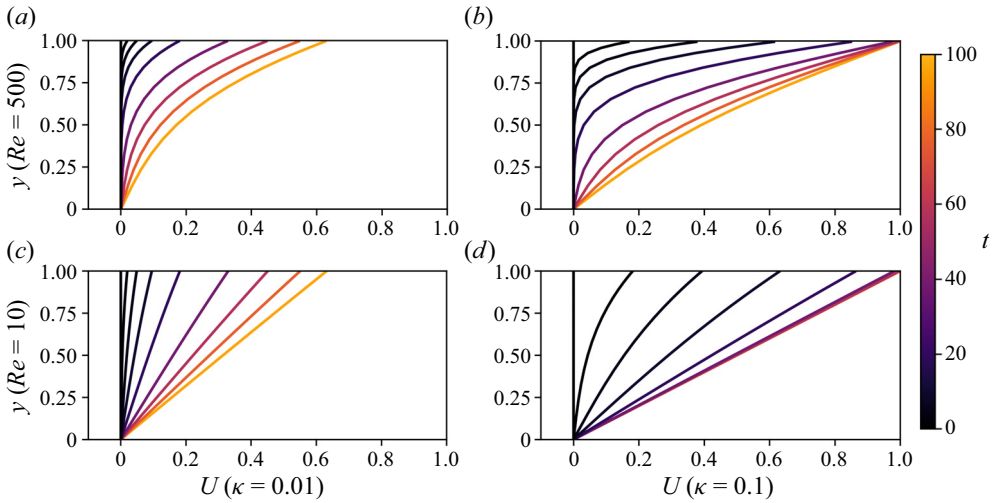
Figure 2. Laminar accelerating WDF. The Reynolds number and acceleration parameter for each flow are noted in the figure. The solution is shown at times $t = [0, 2, 5, 10, 20, 40, 60, 80, 100]$.
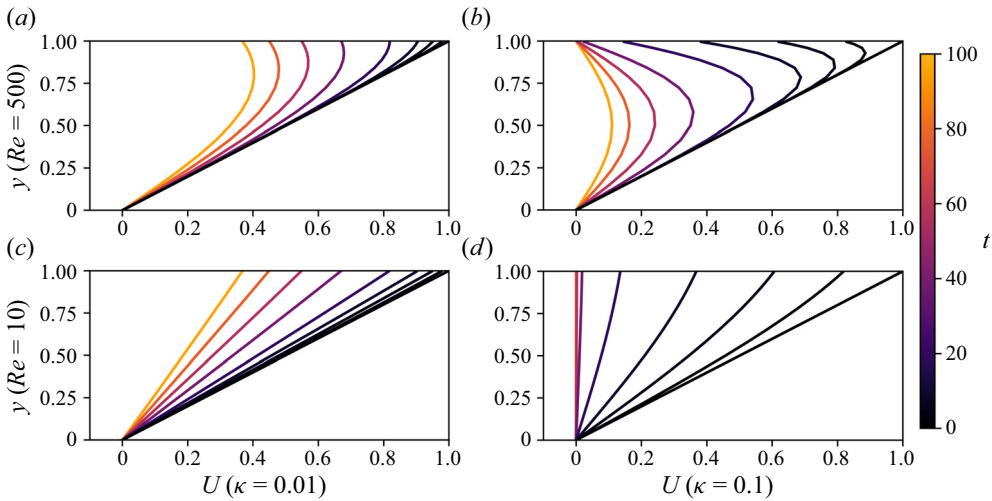

Figure 3. Laminar decelerating WDF. The Reynolds number and deceleration parameter for each flow are noted in the figure. The solution is shown at times $t = [0, 2, 5, 10, 20, 40, 60, 80, 100]$.

Inserting this expression into (2.2)–(2.4) results in an equation for f_p of the form

$$\frac{\partial f_p}{\partial t} + \frac{Re}{2}\frac{\mathrm{d}g_p}{\mathrm{d}t}(y^2 - 1) + \frac{\mathrm{d}g_e}{\mathrm{d}t} = \frac{1}{Re}\frac{\partial^2 f_p}{\partial y^2}, \tag{2.18}$$

with boundary conditions

$$f_p(y = \pm 1, t) = 0 \tag{2.19}$$

and initial condition

$$f_p(y, 0) = h_e - \frac{Re}{2}g_p(0)(y^2 - 1) - g_e(0). \tag{2.20}$$

999 A43-9

To solve (2.18), we represent f_p as

$$f_p(y, t) = \sum_{n=0}^{\infty} \hat{f}_{p,n}(t) \cos\left[\left(n + \frac{1}{2}\right)\pi y\right]. \tag{2.21}$$

The boundary conditions associated with all terms in (2.18) and (2.20) are satisfied by our cosine basis. To solve for the coefficients $\hat{f}_{p,n}(t)$, we repeat the procedure used for WDF. First, we combine (2.21) with (2.18) and take the inner product of the result with $\cos((m + 1/2)\pi y)$ leading to

$$\frac{d\hat{f}_{p,m}}{dt} = \frac{16Re(-1)^m}{(2\pi m + \pi)^3}\frac{dg_p}{dt} - \frac{4(-1)^m}{2\pi m + \pi}\frac{dg_e}{dt} - b_m\hat{f}_{p,m}, \tag{2.22}$$

with $b_m = (2\pi m + \pi)^2/(4Re)$. Solving (2.22) produces

$$\hat{f}_{p,m} = e^{-b_m t}\left[\frac{16Re(-1)^m}{(2\pi m + \pi)^3}\int_0^t e^{b_m t'}\left.\frac{dg_p}{dt}\right|_{t=t'}dt' - \frac{4(-1)^m}{2\pi m + \pi}\int_0^t e^{b_m t'}\left.\frac{dg_e}{dt}\right|_{t=t'}dt' + C_{2,m}\right]. \tag{2.23}$$

Then, to solve for the constant $C_{2,m}$, we take the inner product of the initial condition ((2.20)) with $\cos((m + 1/2)\pi y)$ to obtain

$$C_{2,m} = \int_{-1}^{1}\left[h_e - \frac{Re}{2}g_p(0)(y^2 - 1) - g_e(0)\right]\cos\left[\left(m + \frac{1}{2}\right)\pi y\right]dy. \tag{2.24}$$

If the initial profile is parabolic and there is no wall motion, then $C_2 = 0$. Finally, by inserting $\hat{f}_{p,n}$ into (2.17), we find the laminar profile

$$U(y, t)$$

$$= \sum_{n=0}^{\infty} e^{-b_n t}\left[\frac{16Re(-1)^n}{(2\pi n + \pi)^3}\int_0^t e^{b_n t'}\left.\frac{dg_p}{dt}\right|_{t=t'}dt' - \frac{4(-1)^n}{2\pi n + \pi}\int_0^t e^{b_n t'}\left.\frac{dg_e}{dt}\right|_{t=t'}dt' + C_{2,n}\right]$$

$$\cos\left[\left(n + \frac{1}{2}\right)\pi y\right] + \frac{Re}{2}g_p(t)(y^2 - 1) + g_e(t). \tag{2.25}$$

In Appendix A we provide analytical expressions for the integral in (2.25) for representative flows (see table 1 in Appendix A) and we validate the solution against Womersley flow.

As with the WDF, we study the effect of acceleration and deceleration in the pressure-driven case (here we let $g_e(t) = 0$). A natural first choice for examining the impact of acceleration and deceleration might be to set the pressure gradient to the same profiles used for the wall velocities (i.e. $g_p(t) = 1 - e^{-\kappa t}$ and $g_p(t) = e^{-\kappa t}$). In the case of PDF, we non-dimensionalize the velocity by the maximum centreline velocity. However, the pressure gradient required to satisfy this non-dimensionalization is $g_p = -2/Re$ either at $t = 0$ or as $t \to \infty$. This means that $g_p(t) = 1 - e^{-\kappa t}$ and $g_p(t) = e^{-\kappa t}$ do not properly satisfy the correct profiles, and multiplying these quantities by $-2/Re$ would result in a different pressure gradient profile for different Reynolds numbers.

999 A43-10

Instead of prescribing the same pressure gradient across all cases, we enforce an exponentially decaying accelerating or decelerating flow rate according to

$$Q(t) = \tfrac{2}{3}(1 - e^{-\kappa t}) \tag{2.26}$$

and

$$Q(t) = \tfrac{2}{3}(e^{-\kappa t}), \tag{2.27}$$

respectively. These flow rates correspond to a unit centreline streamwise velocity for a parabolic profile. Note that flow rate and mean velocity are synonymous here. As with wall motion, we delve into the details of this non-dimensionalization in § 2.3.

Prescribing a flow rate requires a corresponding pressure gradient to achieve this flow rate. We first show that accounting for all continuous flow rates requires pressure gradients that can undergo a step change at $t = 0$, after which we compute the pressure gradients g_p and use it to approximate U. We calculate the flow rate by integrating (2.25) in the wall-normal direction and dividing by twice the channel height to result in

$$Q(t) = \sum_{n=0}^{\infty} e^{-b_n t} \left[\frac{32 Re}{(2\pi n + \pi)^4} \int_0^t e^{b_n t'} \left. \frac{dg_p}{dt} \right|_{t=t'} dt' + \frac{2(-1)^n C_{2,n}}{2\pi n + \pi} \right] - \frac{Re}{3} g_p(t). \tag{2.28}$$

Evaluating (2.28) at $t = 0$ and simplifying the resulting expression leads to

$$Q(0) = \sum_{n=0}^{\infty} \frac{2(-1)^n}{2\pi n + \pi} \int_{-1}^{1} h_e(y) \cos \left[\left(n + \frac{1}{2} \right) \pi y \right] dy, \tag{2.29}$$

which shows that the initial flow rate only depends on the initial velocity profile, as expected. Taking the derivative of (2.28), we get after simplifications

$$\frac{dQ}{dt} = - \sum_{n=0}^{\infty} \frac{8}{(2\pi n + \pi)^2} e^{-b_n t} \int_0^t e^{b_n t'} \frac{dg_p(t')}{dt} dt'. \tag{2.30}$$

From this expression, we note that a jump discontinuity is required for g_p as $t \to 0$. If g_p were a continuous function, (2.30) would indicate that $\lim_{t \to 0} dQ/dt = 0$. However, our desired flow rate results in $\lim_{t \to 0} dQ/dt = \pm 2k/3$. Thus, satisfying this derivative constraint necessitates a step change in the pressure gradient at $t = 0$ that can be formulated by

$$g_p(t) = H(t)\hat{g}_0 + \hat{g}_p(t), \tag{2.31}$$

with $H(t)$ as the Heaviside function, $\hat{g}_0$ as a constant and $\hat{g}_p$ as a continuous temporal function. Furthermore, we may use dQ/dt to compute the constant $\hat{g}_0$ by taking the derivative of (2.31) and combining it with 2.30 to produce

$$\lim_{t \to 0} \frac{dQ}{dt} = -\hat{g}_0. \tag{2.32}$$

The above expression indicates that only flow rates with $\lim_{t \to 0} dQ/dt = 0$ can be constructed with a continuous pressure gradient.

Now that we know the form that the pressure gradient must take, we can numerically solve for $g_p(t)$ to satisfy the flow rates given by (2.26) and (2.27). In short, we use the trapezoidal rule on all the integrals and then solve for $g_p(t)$. We include a detailed description of this procedure in Appendix D. In figure 4 we present examples of the
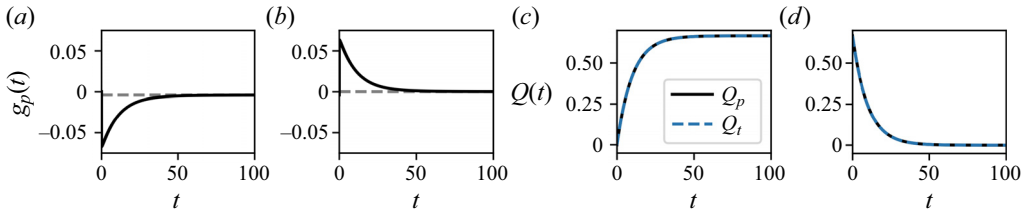
Figure 4. Plots (*a*) and (*b*) are the pressure gradient for flow rates of $Q_t = (2/3)(1 - e^{-\kappa t})$ and $Q_t = (2/3) e^{-\kappa t}$ at $Re = 500$ and $\kappa = 0.1$ (the grey dashed line is the expected long-time value). Plots (*c*) and (*d*) are the flow rates Q_p computed from applying the pressure gradients in (*a*) and (*b*).
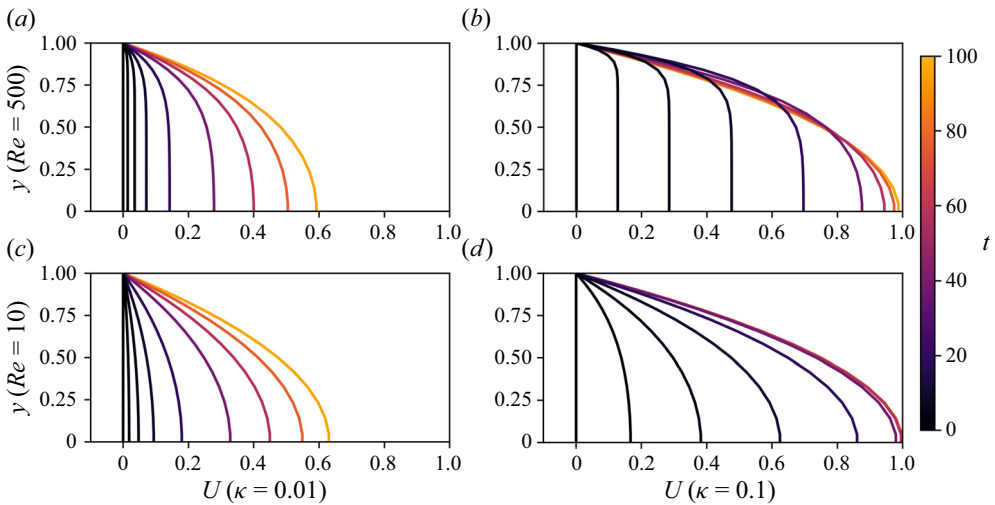

Figure 5. Laminar accelerating PDF. The Reynolds number and acceleration parameter for each flow are denoted in the figure. The solution is shown at times $t = [0, 2, 5, 10, 20, 40, 60, 80, 100]$.

numerically computed pressure gradients and the flow rates of the velocity profiles computed using these gradients at $Re = 500$ and $\kappa = 0.1$. Both pressure gradient profiles start with a constant pressure gradient for achieving zero flow (in the case of acceleration) or a parabolic profile (in the case of deceleration). At start-up, there is a step change in the pressure gradient that subsequently grows or decays toward the pressure gradient needed to maintain the long-time solution. The excellent match of the prescribed flow rates and the computed flow rates in figures 4(*c*) and 4(*d*) validate the computed pressure gradients.

In figure 5 we display the laminar flow solutions with the numerically computed pressure gradient for accelerating cases at $Re = \{10, 500\}$ and $\kappa = \{0.01, 0.1\}$; in figure 6 we show the laminar profiles for decelerating cases with the same parameters. For the accelerating cases, increasing Re and κ produces transient dynamics that are more plug like. For the decelerating cases, the gradient is diminished near the wall compared with the accelerating cases, and at sufficiently high Re and κ, the profile exhibits backflow to maintain the appropriate flow rate. Similar to the decelerating WDF, we show in § 3 that this profile leads to destabilization.

Finally, we emphasize that the solutions provided in (2.14) and (2.25) are applicable for odd and even functions, respectively. Owing to linear superposition, any function may be represented by simply adding the two solutions together. Thus, the solutions presented in
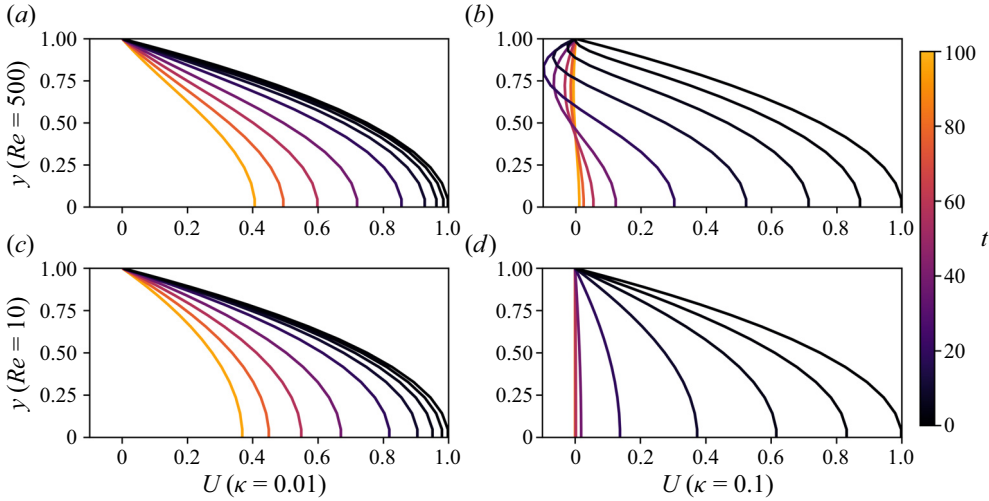
999 A43-12

Figure 6. Laminar decelerating PDF. The Reynolds number and deceleration parameter for each flow are denoted in the figure. The solution is shown at times $t = [0, 2, 5, 10, 20, 40, 60, 80, 100]$.

§§ 2.1 and 2.2 are valid for arbitrary streamwise wall motion and pressure gradients and can accommodate arbitrary wall-normal varying initial conditions.

2.3. *Comments on non-dimensionalization*

Before investigating the stability of these flows, we discuss the non-dimensionalization of the problem set-up. Thus far, the equations presented do not depend on the characteristic velocity U_b. The choice of U_b depends on the selection of the boundary conditions, or pressure gradient, and should be selected to eliminate one of the dimensional parameters driving the flow. To illustrate this point, let us consider the case of accelerating and decelerating wall motion. In dimensional form we may write the velocity at the wall as

$$g_w^*(t) = u_i^* \, e^{-\kappa^* t^*} + u_f^* (1 - e^{-\kappa^* t^*}), \tag{2.33}$$

which, after non-dimensionalization, becomes

$$g_w(t) = u_i \, e^{-\kappa t} + u_f (1 - e^{-\kappa t}), \tag{2.34}$$

with non-dimensional scaling of $u_i = u_i^*/U_b$, $u_f = u_f^*/U_b$ and $\kappa = \kappa^* h/U_b$. As such, the most natural choice for non-dimensionalization is to select a characteristic velocity that forces $u_i = 1$, $u_f = 1$ or $\kappa = 1$. We consider flows that start from rest ($u_i = 0$) or end at rest ($u_f = 0$), so we choose the other velocity as our characteristic velocity U_b and vary the non-dimensional exponential decay parameter κ. Notably, this decay parameter is inversely proportional to the characteristic time scale, for example, the half-life $t_{1/2} = \ln(2)/\kappa$. This suggests that, as we vary Re and κ, we vary two time scales: the time scale over which the fluid in the middle of the channel reacts to wall motion due to viscosity and the time scale over which the wall motion reaches the final velocity. While it may also be possible to consider the viscous time scale, we adopt the advective scale due to the fast motion imposed during the acceleration and deceleration process. The laminar flow depends on both non-dimensional parameters Re and κ, so we must vary both when investigating stability.

In contrast to the WDF, the selection of the characteristic velocity in the pressure-driven case is less obvious. The pressure gradient drives a flow with a characteristic velocity, but it is difficult to determine this characteristic velocity before prescribing the pressure gradient. To address this issue, we instead use the flow rate to determine the characteristic velocity. Additionally, by prescribing an accelerating or decelerating flow rate, we are directly accelerating or decelerating the mean velocity, whereas accelerating or decelerating the pressure gradient has an unclear effect on the mean velocity.

As with wall motion, we non-dimensionalize around either the long-time or the initial profile, which in the case of the accelerating or decelerating profile corresponds to a parabolic profile. This results in the dimensional flow rate equation

$$Q^* = \frac{1}{2h} \int_{-h}^{h} \frac{U(y=0)}{h^2} (h^2 - y^{*2}) \, \mathrm{d}y^*. \tag{2.35}$$

After evaluating the integral and using the non-dimensionalization of $Q = Q^*/U_b$, (2.35) simplifies to

$$Q = \frac{2U(y=0)}{3U_b}. \tag{2.36}$$

We may then set the characteristic velocity as either the final or initial centreline velocity ($U(y=0) = U_b$), which is satisfied when the flow rate is $Q = 2/3$. Thus, we satisfy this non-dimensionalization for the exponentially decaying acceleration and deceleration cases when either Q_∞ or Q_0 equal 2/3 in $Q(t) = Q_\infty(1 - \mathrm{e}^{-\kappa t}) + Q_0 \mathrm{e}^{-\kappa t}$. As we investigate accelerating from rest and decelerating to rest in this work, we only need to sweep over the non-dimensional exponential decay parameter κ.

3. Stability of accelerating and decelerating flows

With the exact laminar solutions for accelerating and decelerating flows established, we proceed to analyse their stability characteristics. As mentioned in § 1, studying the stability of these flows is challenged by the fact that many standard methods provide insight into long-time stability properties, but do not account for a general time dependence of the base flow. To overcome these challenges, we investigate the stability properties of these time-varying base flows via the transient growth of perturbations that evolve according to the linearized NSEs. We start with presenting the linearized equations of motion, which is followed, in § 3.1, with examples of transient growth in our specific application cases. In § 3.2 we then sweep over various wavenumbers, Reynolds numbers and acceleration/deceleration rates to assess the prevalence of transient growth in parameter space. Here we find that higher κ and Re result in a larger energy growth of perturbations, and that decelerating flows exhibit substantially larger growth than constant or accelerating flows. Finally, in § 3.3 we follow the linear evolution of the optimal perturbations through time and verify our results, in § 3.4, against a DNS.

To investigate the evolution of perturbations with respect to a given base flow, we decompose the flow into a laminar base state U and a perturbation u' according to

$$u = U + u', \tag{3.1}$$

where $U = [U, 0, 0]^T$. We then combine (3.1) with (2.1) and assume that $|u'| = O(\epsilon)$ for $0 < \epsilon \ll 1$, which results in the linearized NSEs

$$\frac{\partial U}{\partial t} + g_p - \frac{1}{Re}\nabla^2 U + \frac{\partial u'}{\partial t} + U \cdot \nabla U + U \cdot \nabla u' + u' \cdot \nabla U = -\nabla p' + \frac{1}{Re}\nabla^2 u', \tag{3.2}$$

with $\boldsymbol{g}_p = [g_p, 0, 0]^T$. In the above equation we neglect $O(\epsilon^2)$ terms. Because the laminar solutions found in § 2 satisfy (2.2), the first three terms in (3.2) cancel out, and the fifth term is zero by construction. This simplifies the linearized NSEs such that the only difference between the above equation and the typical form used for time-invariant base flows rests in the time dependency of U. Taking the divergence of (3.2) and combining it with the continuity equation, we can find an equation for the pressure perturbation. Inserting this pressure perturbation back into the wall-normal velocity v' equation yields one equation for v' only. The remaining two momentum equations can be combined into an evolution equation for the wall-normal vorticity $\omega'_y = \partial u'/\partial z - \partial w'/\partial x$, resulting in a system of two equations given as

$$\left(\frac{\partial}{\partial t} + U \frac{\partial}{\partial x} \right) \nabla^2 v' - \frac{\partial^2 U}{\partial y^2} \frac{\partial v'}{\partial x} = \frac{1}{Re} \nabla^4 v' \tag{3.3}$$

and

$$\left(\frac{\partial}{\partial t} + U \frac{\partial}{\partial x} \right) \omega'_y + \frac{\partial U}{\partial y} \frac{\partial v'}{\partial z} = \frac{1}{Re} \nabla^2 \omega'_y, \tag{3.4}$$

with boundary conditions

$$v'(y = \pm 1) = \frac{\partial v'}{\partial y}(y = \pm 1) = \omega'_y(y = \pm 1) = 0. \tag{3.5}$$

We further simplify these equations by seeking streamwise and spanwise periodic perturbations, which introduces the streamwise wavenumbers α and the spanwise wavenumbers β such that

$$v'(x, y, z, t) = \hat{v}(y, t)\, e^{i(\alpha x + \beta z)} \tag{3.6}$$

and

$$\omega'_y(x, y, z, t) = \hat{\omega}_y(y, t)\, e^{i(\alpha x + \beta z)}. \tag{3.7}$$

This assumption results in the set of equations

$$\frac{\partial \hat{v}}{\partial t} = (D^2 - k^2)^{-1} \left[\frac{1}{Re}(D^2 - k^2)^2 - i\alpha U(D^2 - k^2) + i\alpha \frac{\partial^2 U}{\partial y^2} \right] \hat{v} \tag{3.8}$$

and

$$\frac{\partial \hat{\omega}_y}{\partial t} = -i\beta \frac{\partial U}{\partial y} \hat{v} + \left[-i\alpha U + \frac{1}{Re}(D^2 - k^2) \right] \hat{\omega}_y, \tag{3.9}$$

with boundary conditions

$$\hat{v}(y = \pm 1, t) = D\hat{v}(y = \pm 1, t) = \hat{\omega}_y(y = \pm 1, t) = 0, \tag{3.10}$$

where $D = \partial/\partial y$ denotes the wall-normal derivative operator and $k^2 = \alpha^2 + \beta^2$ stands for the wavenumber modulus squared. Rearranging and grouping terms in the above equation

999 A43-15

leads to

$$\frac{\partial}{\partial t}\begin{bmatrix} \hat{v} \\ \hat{\omega}_y \end{bmatrix} = -\mathrm{i}\begin{bmatrix} \mathscr{L}_{os} & 0 \\ \mathscr{L}_c & \mathscr{L}_{sq} \end{bmatrix}\begin{bmatrix} \hat{v} \\ \hat{\omega}_y \end{bmatrix} \tag{3.11}$$

or

$$\frac{\partial \boldsymbol{q}}{\partial t} = -\mathrm{i}\mathscr{L}\boldsymbol{q}, \tag{3.12}$$

with

$$\mathscr{L}_{os} = -(D^2 - k^2)^{-1}\left[\frac{1}{\mathrm{i}Re}(D^2 - k^2)^2 - \alpha U(D^2 - k^2) + \alpha\frac{\partial^2 U}{\partial y^2}\right], \tag{3.13}$$

$$\mathscr{L}_{sq} = \alpha U - \frac{1}{\mathrm{i}Re}(D^2 - k^2) \tag{3.14}$$

and

$$\mathscr{L}_c = \beta\frac{\partial U}{\partial y}. \tag{3.15}$$

The above derivation follows the nomenclature in Reddy & Henningson (1993).

Our goal is to investigate the linear evolution of perturbations through (3.12). This linear equation has solutions of the form

$$\boldsymbol{q}(y, t) = \boldsymbol{A}(t)\boldsymbol{q}(y, 0), \tag{3.16}$$

where $\boldsymbol{A}(t)$ is the fundamental solution operator that satisfies

$$\frac{\partial}{\partial t}\boldsymbol{A}(t) = \mathrm{e}^{-\mathrm{i}\mathscr{L}(t)t}\boldsymbol{A}(t), \qquad \boldsymbol{A}(t = 0) = \boldsymbol{I}. \tag{3.17}$$

In the above, we assume a discretization in the wall-normal y direction that results in a finite-dimensional representation of the fundamental solution in terms of a matrix $\boldsymbol{A}(t)$. Numerically, we approximate $\boldsymbol{A}(t)$ as the finite product of exponentials given by

$$\boldsymbol{A}(n\Delta t) = \Pi_{j=1}^n \mathrm{e}^{-\mathrm{i}\mathscr{L}(j\Delta t)\Delta t}, \tag{3.18}$$

with time step Δt. By computing the approximate solution matrix $\boldsymbol{A}(t)$, we can track the linear evolution and stability characteristics of infinitesimal perturbations. In the following section we use the above formalism to determine the maximum linear growth of perturbations through time.

3.1. *Maximum linear amplification*

Non-normal linear operators can support large levels of transient growth, even though the operator's eigenvalues indicate asymptotic stability (all eigenvalues have negative real parts). We hence investigate this transient behaviour by computing the maximum possible amplification of initial energy density

$$G(t; \alpha, \beta, t_0, Re, \kappa) = \max_{\boldsymbol{q}(t_0) \neq 0}\frac{\|\boldsymbol{q}(t)\|_E^2}{\|\boldsymbol{q}(t_0)\|_E^2} = \max_{\boldsymbol{q}(t_0) \neq 0}\frac{\|\boldsymbol{A}(t)\boldsymbol{q}(t_0)\|_E^2}{\|\boldsymbol{q}(t_0)\|_E^2}, \tag{3.19}$$

where $\|\cdot\|_E$ is the energy norm, the details of which we address below. We refer to the quantity $G(t)$ as amplification or growth. In the above expression, we emphasize that this amplification depends upon the wavenumbers of the perturbation, α and β, the time

horizon $[t_0, t]$ over which the perturbation is observed and the parameters of the base flow Re and κ. For brevity, we omit this explicit parameter dependence in what follows. The transient amplification is taken as the maximum relative increase (or gain) in perturbation energy that can be experienced by any initial perturbation $\boldsymbol{q}(t_0)$ over a given time frame $[t_0, t]$. Notably, a temporal series of $G(t)$ need not arise from the same perturbation $\boldsymbol{q}(t_0)$, but stem from a range of initial perturbations. Consequently, the curve $G(t)$ can be thought of as an envelope bounding the energy amplification of all initial conditions.

A common approach to solving for $G(t)$ is based on the adjoint method (Andersson, Berggren & Henningson [1999](#)). However, when the matrix describing the linearized equations of motion is rather small, it becomes computationally tractable to compute $\boldsymbol{A}(t)$ directly. With $\boldsymbol{A}(t)$ explicitly available, we can capitalize on the fact that (3.19) closely resembles the spectral norm of $\boldsymbol{A}(t)$, which only requires a singular value decomposition. However, as noted above, the energy norm, not the L_2 norm is used in (3.19). For this reason, we must recast this problem as an equivalent L_2-norm problem to proceed.

We define the energy norm according to

$$\|\boldsymbol{q}\|_E^2 = \int_{-1}^{1} (|D\hat{v}|^2 + k^2|\hat{v}|^2 + |\hat{\omega}_y|^2)\, \mathrm{d}y. \tag{3.20}$$

As shown in Gustavsson ([1986](#)), dividing this quantity by $2k^2$ and integrating over all wavenumbers produces the kinetic energy of $\boldsymbol{u}'$. As we consider the relative energy amplification for perturbations at a specific set of wavenumbers, this normalization and integration approach is not necessary for the computation of the growth $G(t)$ (i.e. the normalization constant cancels out in (3.19)). In Appendix B we show how this energy norm can be recast into an equivalent L_2 norm by defining a matrix V such that $\|\boldsymbol{q}\|_E^2 = \|V\boldsymbol{q}\|^2$. We then compute the maximum amplification as

$$G(t) = \max_{\boldsymbol{q}(t_0) \neq 0} \frac{\|V\boldsymbol{A}(t)\boldsymbol{q}(t_0)\|^2}{\|V\boldsymbol{q}(t_0)\|^2} = \max_{\boldsymbol{x}(t_0) \neq 0} \frac{\|V\boldsymbol{A}(t)V^{-1}\boldsymbol{x}(t_0)\|^2}{\|\boldsymbol{x}(t_0)\|^2} = \|V\boldsymbol{A}(t)V^{-1}\|^2, \tag{3.21}$$

where $\boldsymbol{x} = V\boldsymbol{q}$ and the spectral norm of the matrix corresponds to the largest singular value.

In what follows, we compute $G(t)$ by approximating V and $\boldsymbol{A}(t)$ on a grid of $M = 64$ Chebyshev collocation points using a time step of $\Delta t = 0.01$ for both WDF and PDF. We again approximate the base flow with 100 basis functions as in § 2. To illustrate how the amplification varies over time, we consider accelerating and decelerating WDF and PDF at $Re = 500$ and $\kappa = 0.1$ in figures 7 and 8. Note that these laminar profiles were shown in figures 2, 3, 5 and 6.

In figure 7 we plot the amplification $G(t)$ with different parameters for constant, accelerating and decelerating WDF considering strictly streamwise perturbations (figure 7a) and strictly spanwise perturbations (figure 7b). Most notably, streamwise perturbations subjected to the decelerating base flow result in orders of magnitude larger growth than any perturbation of the constant or accelerating flows, both of which only show small growth at early times. Additionally, the largest amplification in the decelerating cases comes from perturbing the flow at early times, but not at $t_0 = 0$. In contrast, the accelerating case exhibits the largest growth for perturbations at later times, when the flow behaves more like a steady flow with a constant profile.

When only spanwise perturbations are considered (figure 7b) the constant profile exhibits the largest amplification of all cases. The accelerating and decelerating cases gradually transition between the amplification of the constant profile and the amplification
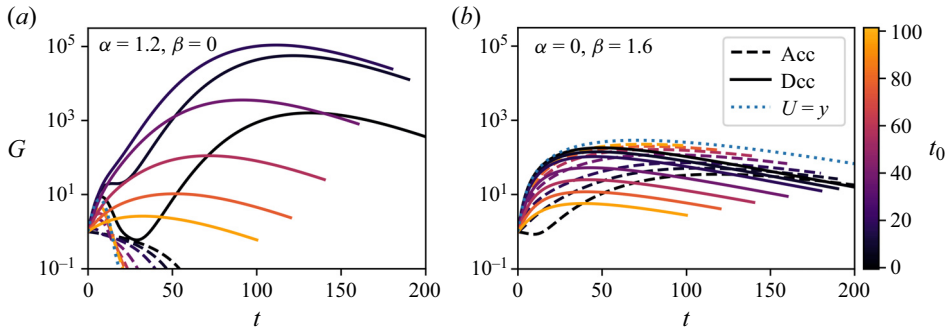
Figure 7. Amplification $G(t)$ for perturbations applied at different times t_0 to accelerating ('Acc'), decelerating ('Dec') and constant WDF at $Re = 500$ and $\kappa = 0.1$. Amplification shown for (a) $[\alpha, \beta] = [1.2, 0]$ and (b) $[\alpha, \beta] = [0, 1.6]$. Perturbations at times $t_0 = [0, 10, 20, 40, 60, 80, 100]$ are shown.
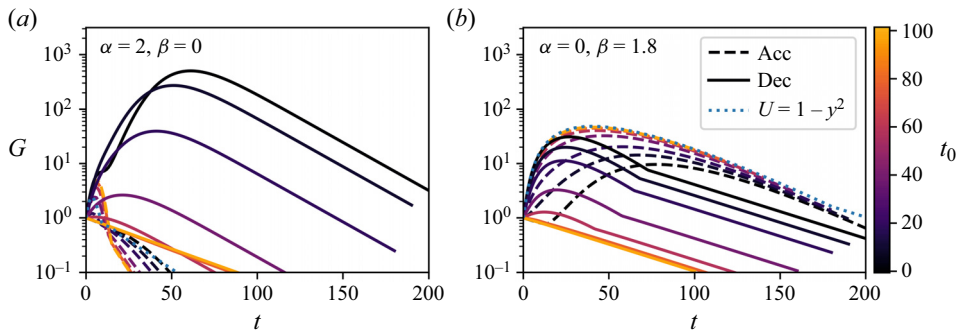

Figure 8. Amplification $G(t)$ for perturbations applied at different times t_0 to accelerating ('Acc'), decelerating ('Dec') and constant PDF at $Re = 500$ and $\kappa = 0.1$. Amplification shown for (a) $[\alpha, \beta] = [2, 0]$ and (b) $[\alpha, \beta] = [0, 1.8]$. Perturbations at times $t_0 = [0, 10, 20, 40, 60, 80, 100]$ are visualized.

in the case of no flow, as the time of the initial perturbation t_0 varies. Naturally, the accelerating case transitions from lower amplification to higher amplification, and the decelerating case transitions from higher amplification to lower amplification, as t_0 increases. This suggests that the shapes of the accelerating and decelerating base flows are less important to the growth of spanwise perturbations.

In figure 8 we show the maximum amplification for constant, accelerating and decelerating PDF. Once again figure 8(a) illustrates that streamwise perturbations about the decelerating base flow exhibit orders of magnitude larger amplification than the other cases, and streamwise perturbations in the constant and accelerating flows experience little growth. In figure 8(b) we again see that spanwise perturbations exhibit the largest amplification for the constant profile, and the accelerating and decelerating cases gradually move between the constant profile and the case of no flow.

Both results for WDF and PDF indicate that perturbations about decelerating laminar base flows may exhibit orders of magnitude greater amplification than perturbations about accelerating or constant laminar profiles. This amplification about decelerating flows occurs predominantly for perturbations with streamwise variations. In contrast, spanwise perturbations lead to the largest energy amplification in constant and accelerating flows.
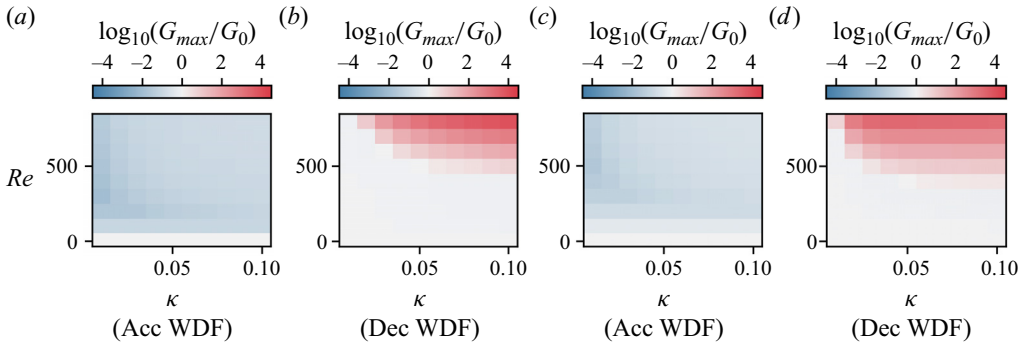
999 A43-18

Figure 9. Maximum growth normalized by the maximum growth of perturbations in the constant flow varied over different Re and κ: (*a*) for accelerating WDF, (*b*) for decelerating WDF, (*c*) for accelerating PDF and (*d*) for decelerating PDF.

3.2. *Maximum growth for accelerating and decelerating flows*

In the previous section we computed $G(t)$ at specific values of Re, α, β and κ. Here, we perform a detailed examination of the maximum growth when sweeping over these parameters for perturbations to the laminar flows at the beginning of the acceleration or deceleration phase at $t_0 = 0$. Although perturbations at later t_0 can exhibit larger growth, the mechanisms of growth at $t_0 = 0$ and at the optimal t_0 tend to be similar in this work. In § 3.5 we further investigate the effect of optimizing over t_0 to illustrate this point. In figure 9 we present the maximum growth $G_{max} = \max_{\alpha, \beta, t} G(t)$ over a set of Re and κ for accelerating and decelerating WDF and PDF. As a point of reference, we normalize the growth by the maximum value G_0 obtained from the constant WDF or PDF case. Both accelerating WDF and PDF exhibit less growth than the constant laminar flow. The growth relative to the constant laminar profile is lowest at the lowest value of κ and moderately low Reynolds number Re. As κ and Re increase, the growth appears to level out at around a tenth of the constant flow.

In contrast to the accelerating laminar cases, the decelerating laminar cases exhibit far larger amplification of perturbations than the constant laminar case. For WDF at $Re = 800$, we see 10^4 times larger amplification over the constant profile. Upon further increasing κ and Re, the relative amplification continues to grow. Decelerating PDF also exhibits this large amplification at high Re and κ.

The two competing factors are the rate κ at which the walls move and the rate at which the flow can react to this motion, i.e. $1/Re$. At large values of κ, the wall motion is fast and the laminar profile is sensitive to changes in Re while insensitive to changes in κ. At the other extreme of small κ, the laminar flows change so slowly that the growth of perturbations behaves similarly to the growth of perturbations in the constant laminar case or the no-flow case.

We focus on this range of Re and κ values because these values show where a transition in growth is exhibited in the decelerating cases. As κ continues to increase, the results converge toward impulsive wall motion (i.e. Stokes' first problem). Similarly, if we continue to increase the Reynolds number, we will find that, at moderate κ values, there is a consistent scaling in the maximum amplification as the Reynolds number changes. Figure 10 shows how G_{max} varies with Re at $\kappa = 0.1$ for constant, accelerating and decelerating WDF and PDF. We also show the Re^2 scaling discussed in Reddy & Henningson (1993) as 'Const Fit' (using the same values) and the best exponential fit for the decelerating cases at $Re > 400$ as 'Dec Fit' ($G_{max} = 0.0015 \times 10^{0.012Re}$ for WDF
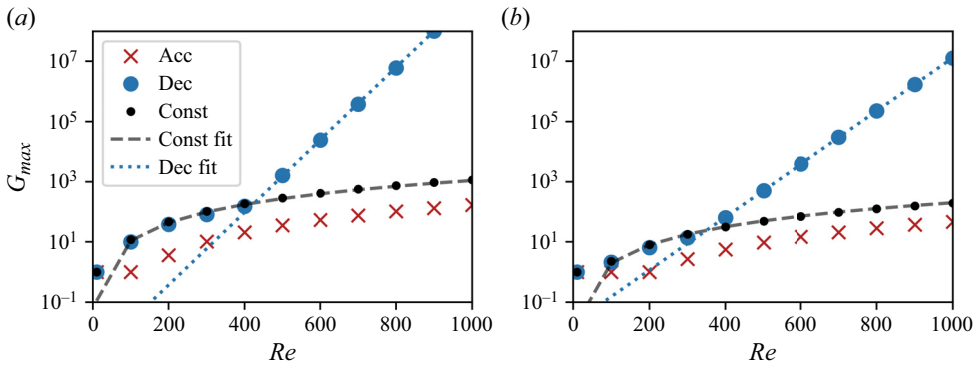
Figure 10. Plots of G_{max} as a function of Re for accelerating flow ('Acc'), decelerating flow ('Dec') and constant flow ('Const') at fixed $\kappa = 0.1$ for (*a*) WDF and (*b*) PDF. The fitting lines are described in the text.

and $G_{max} = 0.0199 \times 10^{0.009Re}$ for PDF). Both the constant and accelerating cases exhibit similar trends over all Reynolds numbers Re, while the decelerating case exhibits two distinct behaviours. At low Re, the decelerating case shows the same Re^2 scaling as the constant case, and at high Re the decelerating case shows a 10^{Re} scaling. As mentioned in § 1, this behaviour was also observed in oscillatory flows shown in Xu *et al.* (2021). However, the optimal perturbations in their work did not exhibit a shift wavenumber as Re increased, which, as we will show, is not the case for these decelerating flows. For low values of Re, viscous forces quickly modify the flow in response to the wall velocity, and the growth behaves similarly to a constant flow. When the Reynolds number is high, the flow reacts more slowly to the wall motion, allowing the laminar base flow to exhibit high curvature, leading to the 10^{Re} scaling. However, unlike the decelerating case, the accelerating case only exhibits the Re^2 scaling. Thus, we must further examine the shape of the perturbations to explain this difference in scaling.

To better understand the cause for decreased amplification in the accelerating case and increased amplification in the decelerating case, we consider the wavenumbers at which the amplification occurs. Figure 11 shows the maximum amplification $\max_t G(t)$ at multiple values of Re, κ, α and β for accelerating WDF. Analogously, figure 12 shows the same results for decelerating WDF. Each figure is normalized by the maximum amplification over all wavenumbers, which is indicated near the top right corner of each plot.

For accelerating WDF, the most amplified perturbations are ones that vary in the spanwise direction at $[\alpha, \beta] \approx [0, 1.6]$. Likewise, the constant laminar profile exhibits maximal amplification for perturbations that vary in the spanwise direction at the same spanwise wavenumber (Reddy & Henningson 1993). Referring back to (3.11), we see that for $\alpha = 0$, $\mathscr{L}_{os}$ and $\mathscr{L}_{sq}$ no longer depend on the laminar base flow. Thus, the influence of the laminar profile only enters through the derivative of the laminar profile in the coupling term $\mathscr{L}_c$. This observation likely explains the weaker dependence on shape exhibited in the amplification shown in figures 7(*b*) and 8(*b*).

Perturbations in decelerating laminar flows exhibit a much different dependency on the wavenumbers as Re and κ vary. At a low rate of deceleration κ, the largest maximum amplification arises from spanwise perturbations. Upon increasing κ, the largest maximum amplification moves towards perturbations with streamwise variations. A similar trend holds for the Reynolds number, such that for $Re = 500$ and $\kappa = 1$, the maximum amplification is due to a streamwise varying perturbation with wavenumbers
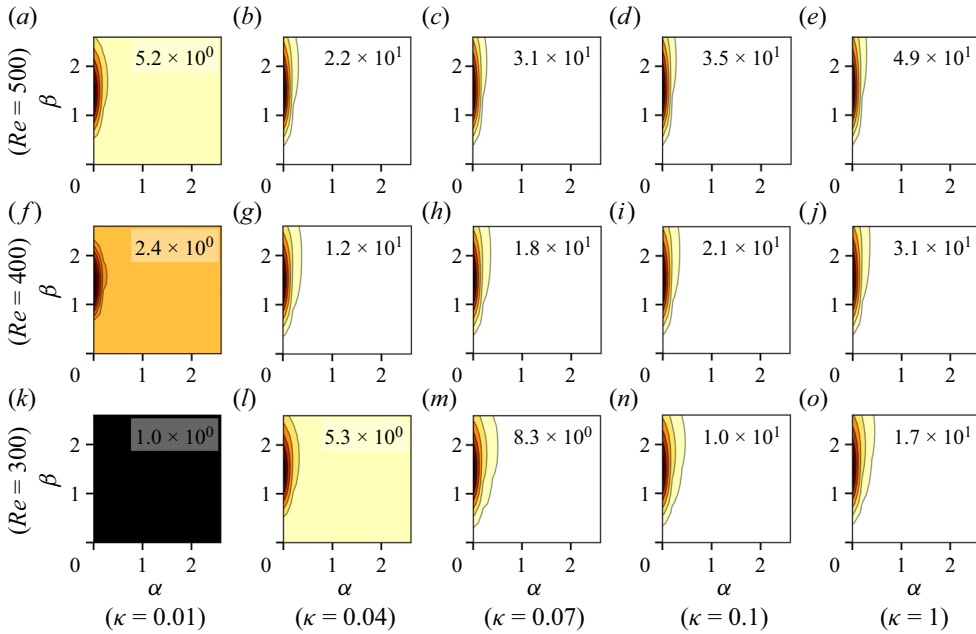
Figure 11. Maximum amplification of perturbations $\max_t G(t)$ for accelerating WDF at different wavenumbers and acceleration rates (denoted in the figure).
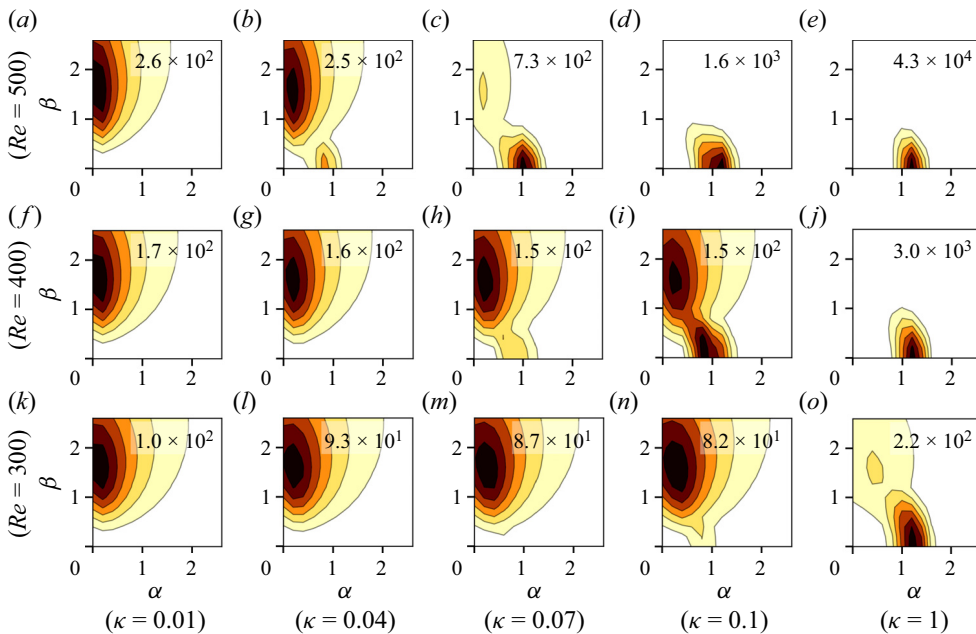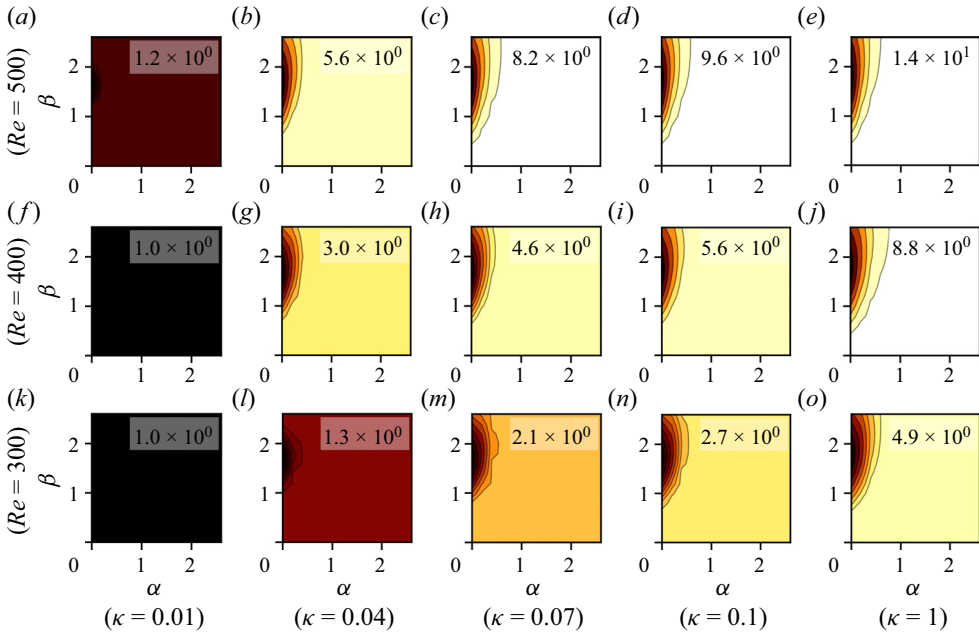

Figure 12. Maximum amplification of perturbations $\max_t G(t)$ for decelerating WDF at different wavenumbers and deceleration rates (denoted in the figure).

$[\alpha, \beta] \approx [1.2, 0]$. Referring back to (3.11), we notice that, for $\beta = 0$, the operator $\mathscr{L}_c$ vanishes, hence decoupling $\hat{v}$ and $\hat{\omega}_y$. Furthermore, spanwise wavenumbers cause $\mathscr{L}_{os}$ and $\mathscr{L}_{sq}$ to both depend on the laminar profile. This indicates that the high levels of

Figure 13. Maximum amplification of perturbations $\max_t G(t)$ for accelerating PDF at different wavenumbers and acceleration rates (denoted in the figure).

amplification to perturbations in the decelerating profiles are directly due to the influence of the velocity and second derivative of the velocity for the decelerating laminar flow, and not due to the interactions between wall-normal velocity and vorticity, as is the case for accelerating and constant profiles.

Next, we investigate the wavenumbers that lead to the largest amplification for accelerating and decelerating PDFs. In figures 13 and 14, we show the maximum amplification for accelerating and decelerating PDFs, respectively. For accelerating flow, there is no growth, or very small growth, at low κ. As κ and Re increase, the maximum amplification increases, and the maximum amplification localizes to spanwise wavenumbers. The maximum amplification occurs at a streamwise wavenumber of $\beta \approx 1.8$, while the constant laminar flow exhibits maximum amplification at a wavenumber of $\beta \approx 2.04$ (Trefethen *et al.* 1993).

In the case of decelerating flow, we again see a gradual shift from spanwise dominant to streamwise dominant perturbations. At low values of κ and Re, the maximum amplification is centred at $[\alpha, \beta] \approx [0, 2.1]$, similar to the constant profile. On the other extreme, i.e. high values of κ and Re, the maximum amplification is centred on streamwise perturbations with a wavenumber of $[\alpha, \beta] \approx [2.2, 0]$. As κ and Re increase, the maximum amplification shifts between these two types of perturbations. Moreover, if the Reynolds number is too low, the maximum amplification will never drift towards streamwise perturbations, and at higher values of Re, the range of κ over which this transition occurs becomes much smaller. This transition is reflected in figure 9 where the maximum growth is plotted vs Re and κ.

3.3. *Structure of optimal perturbations*

In the previous sections we explored how the accelerating laminar flow displays maximum amplification for spanwise perturbations, while the decelerating laminar flow shows
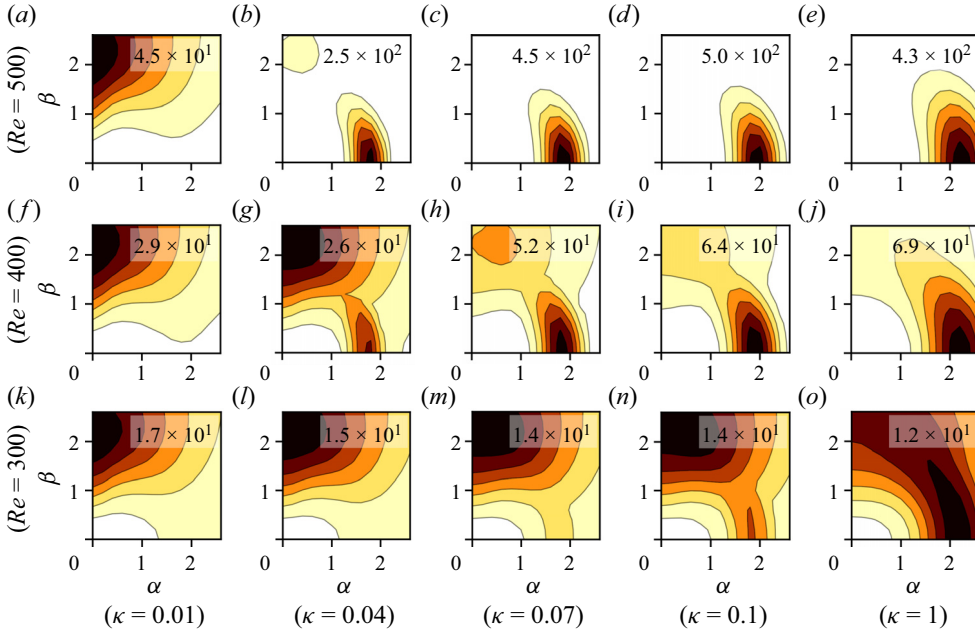
999 A43-22

Figure 14. Maximum amplification of perturbations $\max_t G(t)$ for decelerating PDF at different wavenumbers and deceleration rates (denoted in the figure).

maximum amplification for streamwise perturbations. These results indicate the shape of the maximally amplified perturbation in the periodic coordinate directions, but not in the wall-normal direction. In this section we investigate the structure of the specific perturbations that develop to $\max_t G(t)$. We first outline the calculation of the optimal perturbation and then follow the amplification of that perturbation through time, along with its spatial profile.

For calculating the optimal perturbation, recall that the amplification at some time t' is the energy gain of a perturbation that leads to the largest energy growth over all unit-norm initial perturbations q_0. We compute this quantity by performing the singular value decomposition

$$V\mathbf{A}(t')V^{-1} = \mathbf{U}_S \Sigma \mathbf{V}_S^T, \tag{3.22}$$

where $\mathbf{U}_S$ contains the left singular vectors, $\mathbf{V}_S$ contains the right singular vectors and Σ contains the singular values, ordered by size $\sigma_1 \geq \sigma_2 \geq \cdots \geq \sigma_N$, along its diagonal. The maximum amplification is then given by σ_1^2, and if we consider only the growth along this leading direction we obtain

$$V\mathbf{A}(t')V^{-1}\mathbf{v}_{S,1} = \sigma_1 \mathbf{u}_{S,1}, \tag{3.23}$$

where $\mathbf{u}_{S,1}$ and $\mathbf{v}_{S,1}$ are the principal left and right singular vectors, respectively. The right singular vector $\mathbf{v}_{S,1}$ is transformed via the mapping $V\mathbf{A}(t')V^{-1}$ onto $\mathbf{u}_{S,1}$ and stretched by a factor of σ_1. Owing to this relationship, we conclude that the initial perturbation leading to the maximum amplification at some time t' is given by $\mathbf{v}_{S,1}$. We can subsequently evolve this perturbation in time according to the linearized equations of motion

$$\mathbf{v}(t) = V\mathbf{A}(t)V^{-1}\mathbf{v}_{S,1}, \tag{3.24}$$

and, given $\|\mathbf{v}_{S,1}\|^2 = 1$, we can evaluate the perturbation energy as $G_p(t) = \|\mathbf{v}(t)\|^2$. In what follows, we compute the perturbation $\mathbf{v}_{S,1}$ from time t' at which $G(t)$ is maximized
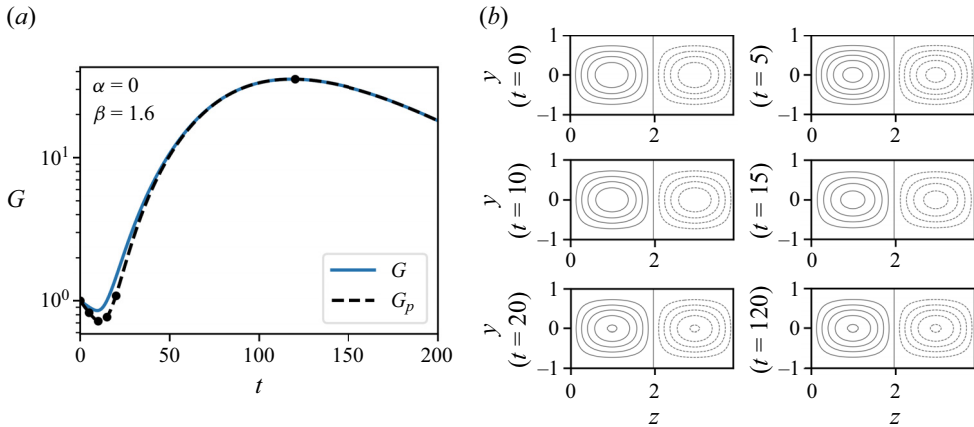
Figure 15. (*a*) Energy of the optimal perturbation and the envelope of growth for accelerating WDF ($Re = 500$, $\kappa = 0.1$). (*b*) Streamfunction of the perturbation as it evolves in time.

($t' = \text{argmax}_t G(t)$). We then display the evolution of the energy and the profile of $\boldsymbol{v}(t)$ through time. It is important to realize that the amplification that maximizes $G(t')$ at some time t' need not necessarily maximize $G(t)$ for any other time.

3.3.1. *Optimal perturbations in WDFs*

First, we consider the accelerating and decelerating WDF cases. In figure 15(*a*) we show the energy of the optimal perturbation over time for accelerating WDF at $Re = 500$ and $\kappa = 0.1$. For this flow, we compute the optimal perturbation that reaches the maximum amplification at $t' = 118$. At short times, the energy of the optimal perturbation falls below the envelope of $G(t)$, and at long times the energy of the optimal perturbation matches $G(t)$. This indicates that other perturbations lead to larger growth at shorter times, but the energy of these perturbations will not reach the long-time energy achieved by the optimal perturbation. In figure 15(*b*) we show the evolution of the perturbation at the times indicated in figure 15(*a*). We visualize the perturbation with contours of the streamfunction. The perturbation takes the form of streamwise vortices that initially decay in magnitude, but subsequently grow as the flow accelerates towards the simple shear profile. The shape of this perturbation closely resembles that of the optimal perturbation in constant WDF and grows via a 'vortex-tilting' mechanism (Butler & Farrell 1992). Unlike constant WDF, the perturbation in the accelerating flow exhibits an initial drop in energy due to the transient period in which the accelerating profile develops towards the simple shear profile.

The dynamics of the perturbation in the decelerating case behave much differently from the constant WDF. Figure 16(*a*) shows the energy of the optimal perturbation for decelerating WDF and the largest real part of the eigenvalue of the time-varying linear operator λ_{max} at $Re = 500$ and $\kappa = 0.1$. In this case, we compute the optimal perturbation that reaches its maximum amplitude at $t' = 132$. Similar to the accelerating case, the energy of the perturbation falls below $G(t)$ at early times but matches $G(t)$ at long times. Unlike the accelerating case, the perturbation in the decelerating case exhibits initial growth, followed by decay, before growing again to reach much larger energy values. Notably, the second peak in the growth begins when the instantaneous eigenvalue becomes positive and decays when the eigenvalue becomes negative.
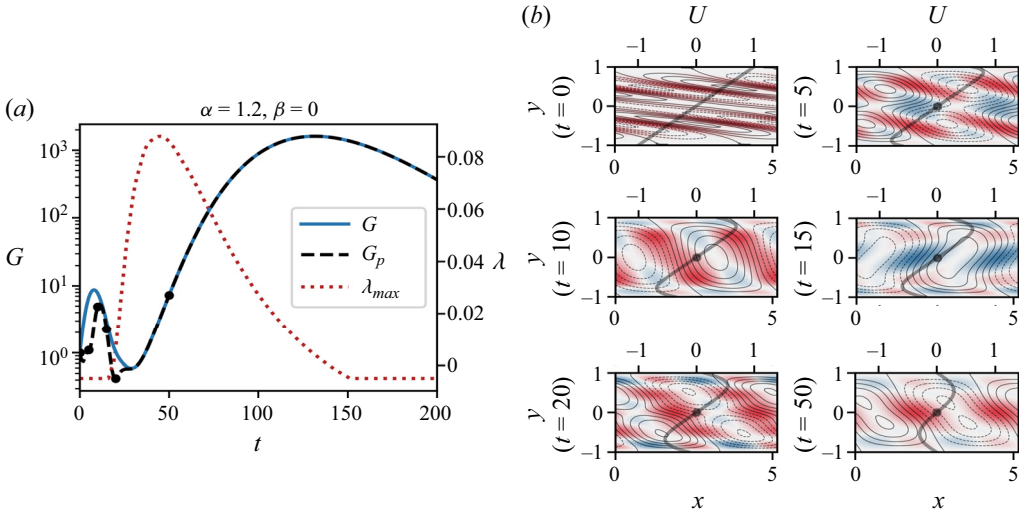
999 A43-24

Figure 16. (*a*) Energy of the optimal perturbation, the envelope of growth and the instantaneous eigenvalue for decelerating WDF ($Re = 500$, $\kappa = 0.1$). (*b*) Thin lines are the streamfunction of the perturbation as it evolves in time. The filled contour plot visualizes the production ((3.25)) normalized by the maximum absolute value (red indicates positive values and blue indicates negative values). The thick black line is the reference laminar profile (U), with a dot at the inflection point.

Along with the energy of the optimal perturbation, in figure 16(*b*) we show the evolution of the optimal perturbation for decelerating WDF. We also plot the laminar profile and the spatial energy production

$$P = -u'v'\frac{\partial U}{\partial y}, \tag{3.25}$$

to identify the cause of energy growth. Note that this term lies in the production term of the energy equation (Serrin 1959; Conrad & Criminale 1965)

$$\frac{\mathrm{d}E}{\mathrm{d}t} = \frac{\mathrm{d}}{\mathrm{d}t}\int_V \frac{\boldsymbol{u}'\cdot\boldsymbol{u}'}{2}\,\mathrm{d}V = -\int_V \frac{1}{Re}\nabla^2\boldsymbol{u}':\nabla^2\boldsymbol{u}'\,\mathrm{d}V - \int_V \boldsymbol{u}'\cdot\boldsymbol{\nabla}U\cdot\boldsymbol{u}'\,\mathrm{d}V. \tag{3.26}$$

In the inviscid case, for a *y*-dependent streamwise baseflow, this equation simplifies to

$$\frac{\mathrm{d}E}{\mathrm{d}t} = \int_V -u'v'\frac{\mathrm{d}U}{\mathrm{d}y}\,\mathrm{d}V = \int_V \frac{\partial\psi}{\partial y}\frac{\partial\psi}{\partial x}\frac{\mathrm{d}U}{\mathrm{d}y}\,\mathrm{d}V = \int_V -\left.\frac{\mathrm{d}y}{\mathrm{d}x}\right|_\psi \frac{\mathrm{d}U}{\mathrm{d}y}\,\mathrm{d}V, \tag{3.27}$$

where ψ represents the streamfunction. Thus, energy increases when the term under the integral is negative or when the streamlines align opposite to the gradient of the laminar flow. This mechanism of growth is referred to as the Orr mechanism or the down-gradient Reynolds stress mechanism in Butler & Farrell (1992).

At $t = 0$ the streamfunction of the initial perturbation opposes the laminar shear, causing the initial gain in energy. The streamlines are advected by the laminar profile causing them to rotate and break up at $t = 2$ and $t = 5$. Over this time window, the energy grows. Then, at $t = 10$ the streamlines become vertical and eventually align with the laminar shear at $t = 15$ causing the energy to decrease. Finally, the streamlines once again advect and align opposite to the laminar shear, over much of the domain, causing the energy to increase. After $t \approx 50$, there is little change in the shape of the perturbation, which we show at $t = 70$.
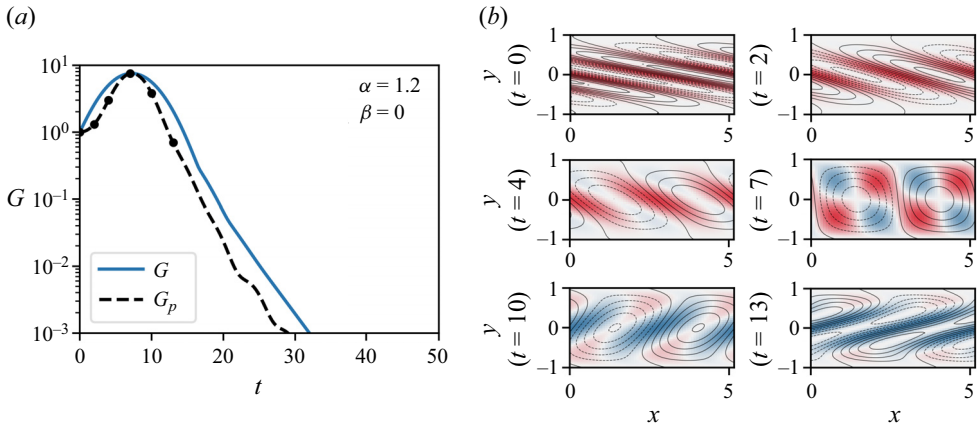
Figure 17. (*a*) Energy of the optimal perturbation and the envelope of growth for constant WDF (*Re* = 500). (*b*) Thin lines are the streamfunction of the perturbation as it evolves in time. The filled contour plot visualizes the production ((3.25)) normalized by the maximum absolute value (red is positive and blue is negative).

Throughout this time series, the energy production follows the anti-aligned streamlines supporting the claim that the Orr mechanism is responsible for this energy growth. In Morón, Feldmann & Avila (2022) the production was also shown to coincide with the inflection point for pulsatile flows. For WDF, the inflection point always remains in the centre of the channel. At early times, the location of the inflection point does not match energy production, but, at later times, energy is produced at the inflection point. It remains unclear if the inflection point plays an important role in our understanding of the stability of this problem. One approach to further investigate the significance of the inflection point could be to use a master-slave model that eliminates this inflection point, as was performed in Morón & Avila (2024).

Next, we show why this Orr mechanism leads to minimal growth in accelerating and constant WDFs. figure 17 shows the energy and evolution of the optimal perturbation for constant WDF at the same wavenumbers as in the decelerating case and for $t' = 7.25$. The perturbation in constant WDF reaches a similar amplification to the first peak in the decelerating case, but then rapidly dies off. Figure 17(*b*) shows the evolution of this perturbation. The initial perturbation closely resembles the perturbation in the decelerating case, and it follows a similar evolution up to $t = 7$ wherein the streamlines initially oppose the laminar shear before aligning vertically. However, in contrast to the decelerating case, the constant laminar profile rotates the streamlines and retains this alignment with the laminar shear causing the energy of the perturbation to drop drastically, as shown at $t = 10$ and $t = 13$.

We emphasize the key difference in the evolution of the decelerating flow and the accelerating or constant flow is this long-time alignment of the streamfunction. Streamwise perturbations in decelerating flows exhibit large growth because the streamfunction aligns opposite to the laminar shear. Streamwise perturbations in accelerating or constant flows exhibit small growth because the streamfunction aligns with the laminar shear. Thus, a key conclusion of our results is that there is a range of critical Reynolds numbers and deceleration rates where the optimal perturbations switch from spanwise to streamwise perturbations for decelerating flows. This transition occurs when growth due to vortex tilting is outpaced by growth due to the Orr mechanism. Once the Orr mechanism dominates, the maximum amplification scales exponentially with the Reynolds number resulting in massive amplification not experienced in accelerating or constant flows.
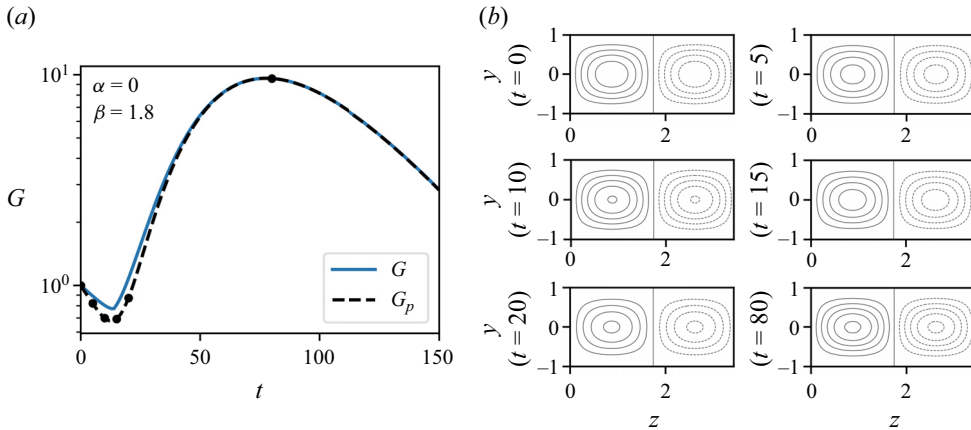
999 A43-26

Figure 18. (*a*) Energy of the optimal perturbation and the envelope of growth for accelerating PDF ($Re = 500$, $\kappa = 0.1$). (*b*) Streamfunction of the perturbation as it evolves in time.

3.3.2. *Optimal perturbations in PDFs*

Next, we turn toward the accelerating and decelerating PDF cases. Figure 18(*a*) shows the energy of the optimal perturbation for accelerating PDF at $Re = 500$ and $\kappa = 0.1$. Here, the optimal perturbation reaches the maximum amplitude at $t' = 78$. Qualitatively, an accelerating PDF shows the same characteristics as an accelerating WDF. The energy of the perturbation initially drops and then increases as the flow accelerates, and the perturbations again take the form of streamwise vortices. Figure 18(*b*) shows the evolution of the perturbation at the times indicated in figure 18(*a*). Again, the shape of this perturbation comes in the form of streamwise vortices, which agrees with the constant PDF case in Butler & Farrell (1992).

Lastly, we consider the case of decelerating PDF. In figure 19(*a*) we show the energy of the optimal perturbation that maximizes $G(t')$ at $t' = 61$. Unlike the previous cases, even at short times the energy of the perturbation closely follows the envelope over all perturbations $G(t)$. The decelerating PDF does not exhibit a drop in energy, as seen in the decelerating WDF, because λ_{max} becomes positive sooner. figure 19(*b*) shows the evolution of the optimal perturbation corresponding to the points in figure 19(*a*). Again, we show the laminar profile for reference. Similar to the decelerating WDF case, the initial profile opposes the laminar shear leading to growth. As this perturbation evolves, it is advected downstream and the streamfunction orients vertically, which momentarily damps growth. Then, the perturbation again aligns opposite to the laminar shear and stops moving as the base profile tends towards no flow. For constant PDF, the streamwise perturbations damp out rapidly (Butler & Farrell 1992), but here the time-varying nature of the base flow allows the perturbation to align opposite to the flow and experience extended periods of growth. Again, we see that the energy is produced at the locations of anti-alignment with the laminar shear. Unlike the WDF case, this production tends to stay near the wall-normal location of the inflection points, similar to Morón *et al.* (2022).

3.4. *Nonlinear evolution of perturbations*

Thus far, we have shown the evolution of perturbations through the linearized equations of motion. In this section we investigate the evolution of optimal perturbations in DNS and the role of these optimal perturbations when perturbing the flow with random noise.
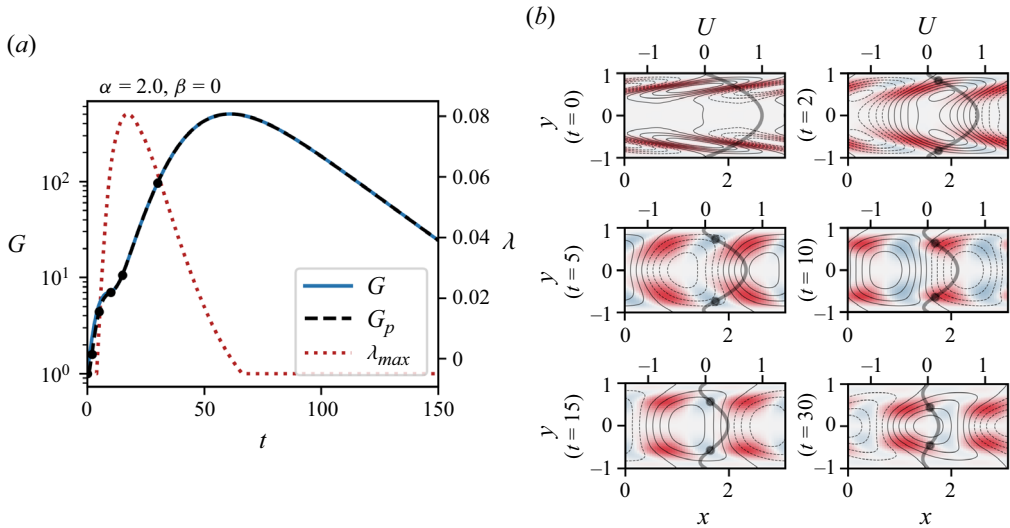
Figure 19. (*a*) Energy of the optimal perturbation, the envelope of growth and the instantaneous eigenvalue for decelerating PDF ($Re = 500$, $\kappa = 0.1$). (*b*) Thin lines are the streamfunction of the perturbation as it evolves in time. The filled contour plot visualizes the production ((3.25)) normalized by the maximum absolute value (red indicates positive, blue indicates negative values). The thick black line is the reference laminar profile (U), with a dot at the inflection point.

We perform DNS of decelerating WDF and PDF at $Re = 500$ and $\kappa = 0.1$ Our DNS uses a Fourier–Chebyshev pseudo-spectral code implemented in Python (Linot, Zeng & Graham 2023*a*,*b*), which is based on the Channelflow code developed by Gibson (2012), Gibson *et al.* (2021). We use the Spalart-Moser Runge–Kutta (SMRK2) scheme (Spalart, Moser & Rogers 1991) to integrate solutions forward in time. This is a multistage scheme that treats the linear term implicitly and the nonlinear term explicitly. The SMRK2 scheme only requires one flow field at one instant in time, which we require to satisfy the decelerating boundary condition at every time step. In the case of PDF we directly impose the exponentially decaying flow rate, not the numerical estimate of the pressure gradient shown in figure 4. For more details on the implementation of the DNS, we refer the reader to Linot *et al.* (2023*b*) and Gibson (2012).

First, we validate the results of the DNS by showing that it maintains the analytical laminar profiles. Here, we perform simulations with a time step of $\Delta t = 0.01$ on a grid size of $[N_x, N_y, N_z] = [2, 81, 2]$ and a domain of $[L_x, L_y, L_z] = [1, 2, 1]$ with no noise. As the laminar flow only varies in the wall-normal direction, the choice of $N_x = 2$ and $N_z = 2$ was chosen to speed up the computation. Using more grid points in these directions does not influence the results. Figure 20 compares the laminar solutions derived in § 2 to the DNS, showing that the DNS and the laminar solution are in excellent agreement.

Next, we consider the effect of applying the optimal perturbations to both of these flows. In both cases, the optimal perturbations are predominantly streamwise structures. Due to this two dimensionality, we perform the DNS on a grid of size $[N_x, N_y, N_z] = [32, 81, 2]$ and a domain size of $[L_x, L_y, L_z] = [2\pi/\alpha_{opt}, 2, 1]$ with a time step of $\Delta t = 0.01$. Simulating on more grid points in the spanwise direction does not change the results, since the initial perturbation does not vary in this direction. We initialize both DNS with an initial condition $\boldsymbol{u} = \boldsymbol{U} + \boldsymbol{u}'$, where we reduce the magnitude of the optimal perturbations shown in figures 16(*a*) and 19(*a*), such that $\boldsymbol{u}' = 10^{-3}\boldsymbol{u}'_p$. With this
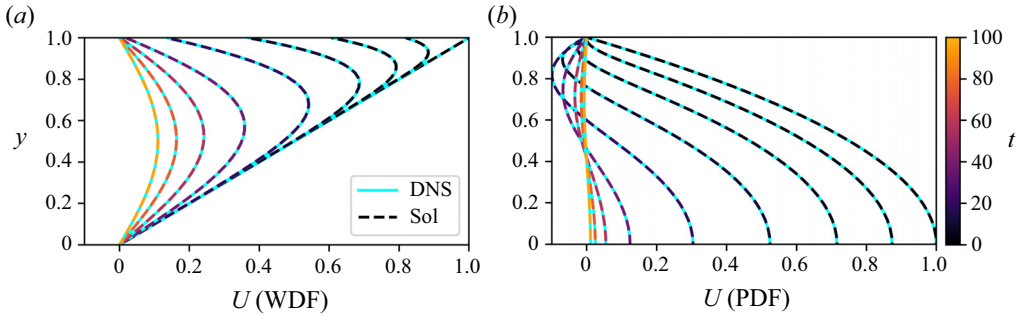
999 A43-28

Figure 20. Analytical and DNS solutions for laminar (*a*) WDF and (*b*) PDF at $Re = 500$ and $\kappa = 0.1$.
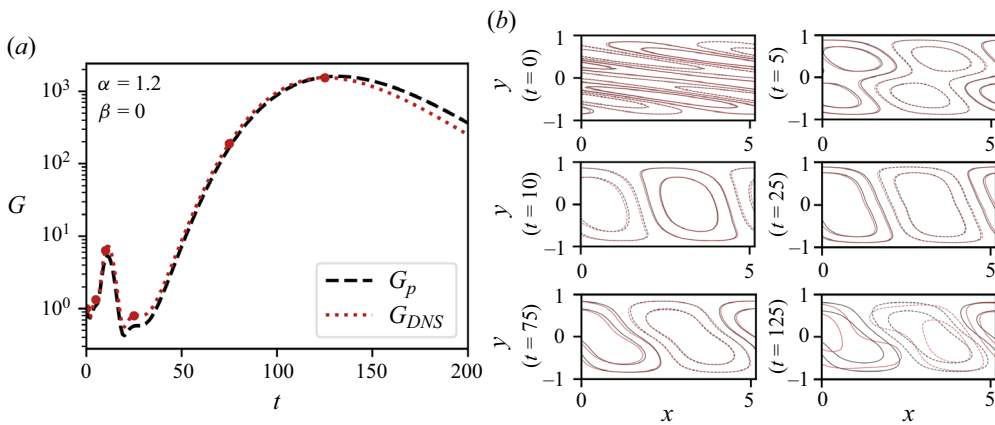

Figure 21. (*a*) Energy of the optimal perturbation for decelerating WDF ($Re = 500$, $\kappa = 0.1$) determined by the linearized equations of motion G_p and by the DNS G_{DNS}. (*b*) Streamfunction of the perturbation as it evolves in time (black is from the linearized equations and red is from the DNS).

initialization the energy ratio of the perturbation is $\|\boldsymbol{u}'\|_E^2/\|\boldsymbol{U}\|_E^2 = O(10^{-7})$ in both cases. Figure 21 displays, for WDF, the energy of the perturbation from the DNS, and the shape of the perturbation as it evolves in time. The energy in the DNS matches the linearized solution extremely well until $t \approx 125$, at which point the energy of the DNS starts to drop more rapidly. At $t = 125$, the energy ratio of the perturbation is $\|\boldsymbol{u}'\|_E^2/\|\boldsymbol{U}\|_E^2 \approx 0.11$ due to the reduced energy in the laminar profile and the growth of the perturbation. The sizeable portion of energy contribution from the perturbation suggests that the assumption of linearity at this point likely breaks down. In figure 21(*b*) we show the evolution of the perturbation through time. Until $t \approx 75$, we see excellent agreement between the optimal perturbation computed via the linearized equations and the DNS. As mentioned, after this time the relative size of the perturbation becomes sufficiently large, and nonlinear effects distort the field, as shown in the final snapshot at $t = 125$.

In figure 22 we show the optimal perturbation in a DNS of PDF. Again, the energy of the DNS agrees well with the energy of the solution in the linearized equations at early times and begins to deviate around $t = 50$. At the peak of $t = 60$, the energy ratio of the perturbation is $\|\boldsymbol{u}'\|_E^2/\|\boldsymbol{U}\|_E^2 \approx 0.03$. Figure 22(*b*) shows the evolution of the perturbation through time. Here, the perturbation in the DNS remains similar to the evolution in the linearized equations, even when the energy starts to differ at $t = 60$.
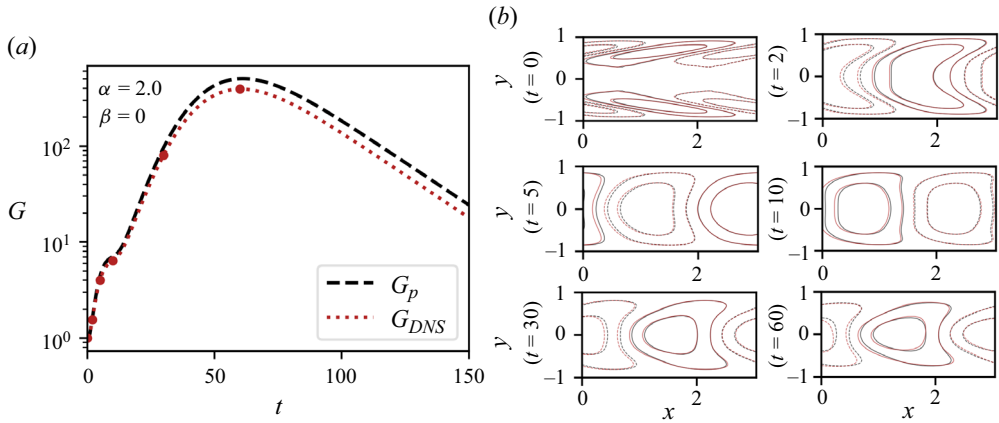
999 A43-29

Figure 22. (*a*) Energy of the optimal perturbation for decelerating PDF ($Re = 500$, $\kappa = 0.1$) determined by the linearized equations of motion G_p and by the DNS G_{DNS}. (*b*) Streamfunction of the perturbation as it evolves in time (black indicates the linearized equations and red is from the DNS).
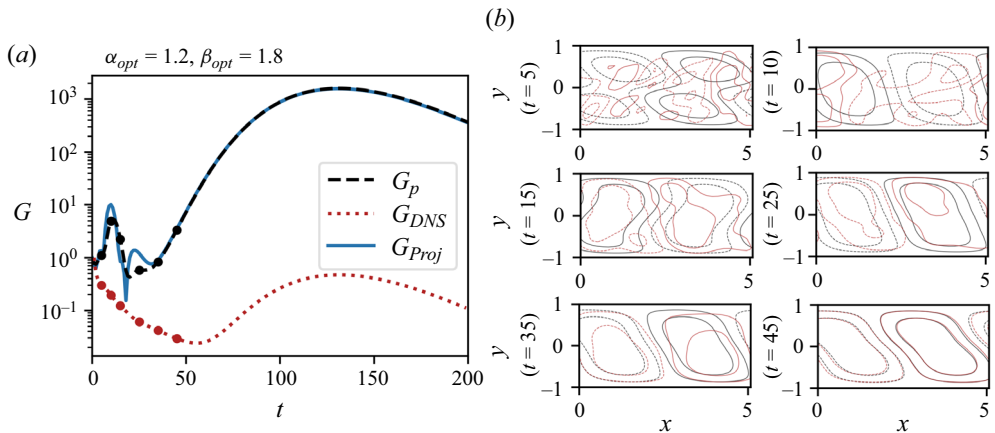

Figure 23. (*a*) Energy of the optimal perturbation for decelerating WDF ($Re = 500$, $\kappa = 0.1$) determined by the linearized equations of motion G_p and energy of a random perturbation in a DNS G_{DNS}, along with the energy of the random perturbation projected onto the optimal perturbation G_{Proj}. (*b*) Streamfunction of the perturbation as it evolves in time (black is from the linearized equations and red is from the DNS).

We have established that the optimal perturbation exhibits large growth even in a DNS. As a next step, we investigate the relevance of this growth in the presence of random perturbations. We perform DNS on a grid of size $[N_x, N_y, N_z] = [32, 81, 32]$ and a domain size of $[L_x, L_y, L_z] = [2\pi/\alpha_{opt}, 2, 2\pi/\beta_{opt}]$ with a time step of $\Delta t = 0.01$. Here, we chose β_{opt} as the strictly spanwise perturbation that causes the largest amplification for $\kappa = 0.1$ and $Re = 500$. This choice of domain size allows the largest growing spanwise and streamwise perturbations to grow simultaneously. We then perturb this flow with Gaussian noise at every grid point such that $\boldsymbol{u}' \sim \mathcal{N}(0, \varepsilon^2)$, where $\varepsilon = 10^{-7}$. Even though this noise is initially not incompressible, the DNS enforces incompressibility after the first time step.

In figure 23(*a*) we show the energy of the optimal perturbation, the randomly perturbed field and the projection of the random perturbation onto the optimal perturbation for WDF at $Re = 500$ and $\kappa = 0.1$. The random perturbation exhibits a decay in energy until $t \approx 50$, followed by a growth in energy that peaks when the energy of the optimal perturbation peaks. At early times, this energy decay occurs because most modes decay, despite
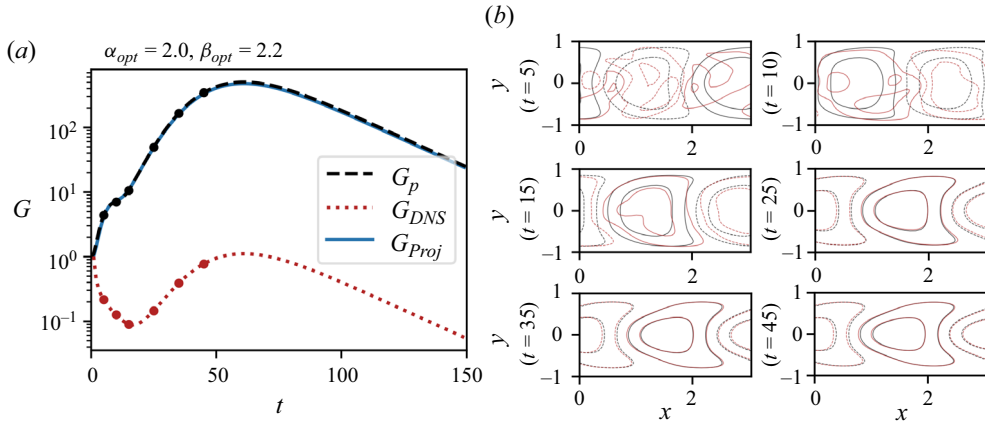
999 A43-30

Figure 24. (*a*) Energy of the optimal perturbation for decelerating PDF ($Re = 500$, $\kappa = 0.1$) determined by the linearized equations of motion G_p and energy of a random perturbation in a DNS G_{DNS}, along with the energy of the random perturbation projected onto the optimal perturbation G_{Proj}. (*b*) Streamfunction of the perturbation as it evolves in time (black is from the linearized equations and red is from the DNS).

the energy associated with the optimal perturbation growing. It is not until later in the evolution of this noise that the optimal perturbation can grow sufficiently large to increase the energy of the random perturbation. The projection of the random perturbation onto the optimal perturbation shows that despite the drop in energy of the overall perturbation, the part associated with the optimal perturbation exhibits the expected growth. The slight mismatch between the projection and the energy of the optimal perturbation is conjectured to come from interactions between the modes, as they do not remain orthogonal during their temporal evolution. We also show the evolution of the random perturbation in figure 23(*b*). The random perturbation differs substantially from the optimal perturbation at early times, but begins to tilt against the laminar shear at $t \approx 25$, before exhibiting close agreement with the optimal perturbation at $t \geq 45$. We compute the streamlines for the random perturbation assuming the flow is two dimensional at $z = 0$. Choosing a different z location would influence the field at early times, but the random field becomes a streamwise perturbation, like the optimal perturbation, at later times.

Figure 24 shows the same results for PDF at $Re = 500$ and $\kappa = 0.1$. The energy of the random perturbation decreases until $t \approx 16$ before increasing and peaking at the same time as the optimal perturbation. Due to the faster time scale over which growth happens in this case, the projection of the random perturbation onto the optimal perturbation matches the energy of the optimal perturbation even at early times. Furthermore, the streamlines of the random perturbation agree with those of the optimal perturbation at $t \geq 25$. These figures show that, despite exhibiting far less growth, the random perturbation evolves into the optimal perturbation.

3.5. *Optimal perturbation timing*

Up to this point we have predominantly considered perturbations applied at the first instant of acceleration or deceleration. However, as noted in figures 7 and 8, perturbations can grow larger when applied at later times. In this section we investigate this behaviour by sweeping over the time t_0 when we apply the perturbation. Figure 25 shows the maximum amplification $G_{max,t_0} = \max_{\alpha,\beta,t,t_0} G(t)$ and the time at which the perturbation is applied at various Re and κ for decelerating WDF and PDF. Similar to the results in figure 9, there
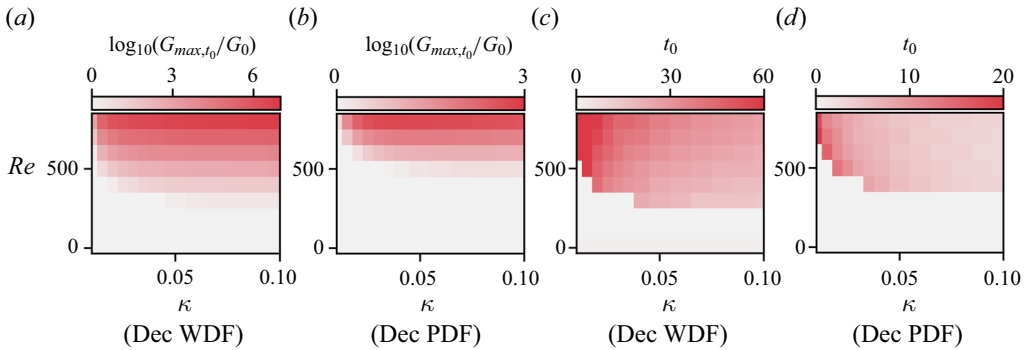
Figure 25. Panels (*a*) and (*b*) show the maximum growth normalized by the maximum growth of perturbations in the constant flow at various Re and κ for decelerating WDF and decelerating PDF. Panels (*c*) and (*d*) show the optimal perturbation timing at various Re and κ for decelerating WDF and decelerating PDF.
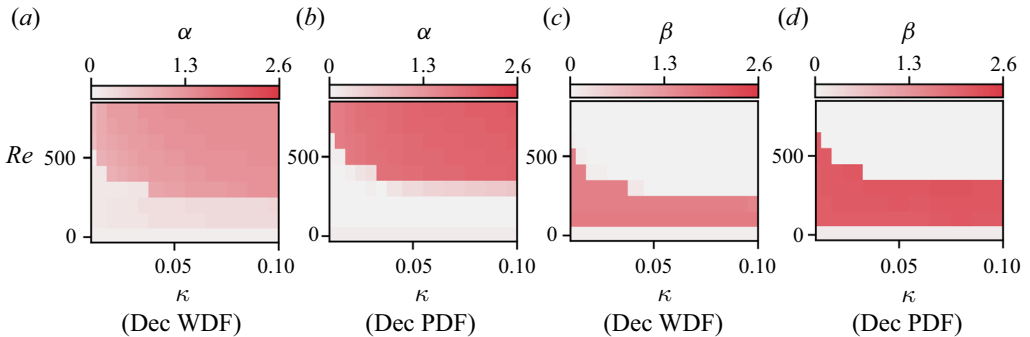

Figure 26. Panels (*a*) and (*b*) show the optimal perturbation streamwise wavenumber at various Re and κ for decelerating WDF and decelerating PDF. Panels (*c*) and (*d*) show the optimal perturbation spanwise wavenumber at Re and κ for decelerating WDF and decelerating PDF.

is a massive increase in the amplification as Re and κ increase. For WDF, this increase in amplification now appears at lower values of both Re and κ, in comparison to the $t_0 = 0$ case. Figures 25(*c*) and 25(*d*) show that this increase coincides with a substantial delay in the application of the perturbation. At low κ, this delay is largest, and decreases and converges as κ increases. When κ is small, the time scale associated with wall motion dominates; when κ is large, the viscous time scale dominates.

In figure 26 we show the optimal wavenumbers at which G_{max,t_0} is achieved. Qualitatively, these results agree with the results at $t_0 = 0$. At low κ and Re, the optimal perturbations are spanwise with $\beta \approx 1.6$ for WDF and $\beta \approx 2.2$ for PDF. At high Re, the optimal perturbations are streamwise with $\alpha \approx 0.8$, at low κ, and $\alpha \approx 1.4$, at high κ, for WDF. In PDF the optimal perturbations are at $\alpha \approx 1.6$, at low κ, and $\alpha \approx 2.1$, at high κ. Again, this highlights that branch switching occurs at sufficiently high Re and κ.

Next, we investigate the shape of the optimal perturbations at the optimal timing and inform the results with linear stability analysis using the quasi-steady state approximation. Figure 27(*a*) shows the energy of the optimal perturbation, the real part of the largest instantaneous eigenvalue and the energy of evolving different eigenvectors forward in time for WDF at $Re = 500$ and $\kappa = 0.1$. Figure 27(*b*) shows the evolution of the optimal perturbation and the eigenvectors of the instantaneous linear operator at various times for WDF. This figure highlights three important times in the evolution of the optimal perturbation. First, the initial phase of the optimal perturbation occurs around when
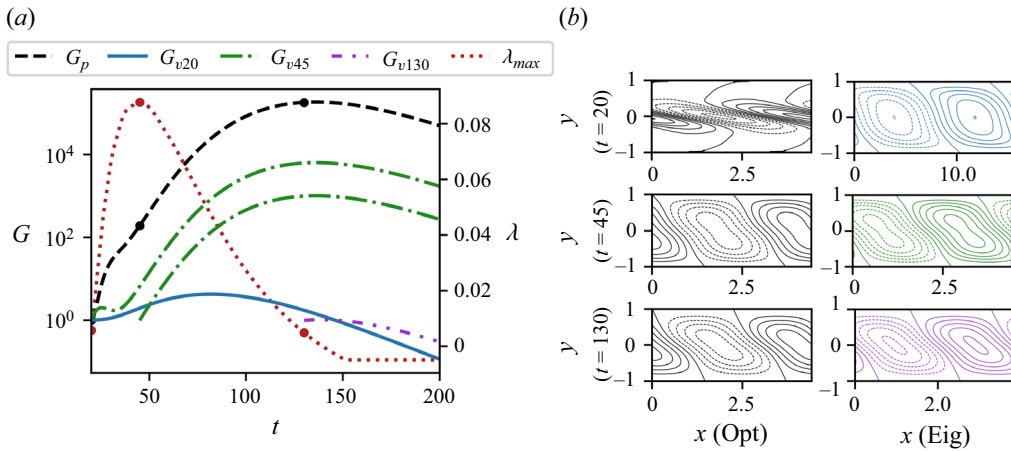
999 A43-32

Figure 27. (*a*) Evolution of the optimal perturbation and of eigenvectors of the instantaneous linear operator for decelerating WDF ($Re = 500$, $\kappa = 0.1$) determined by the linearized equations of motion and the largest eigenvalue of the instantaneous linear operator. (*b*) Streamfunction of the perturbation as it evolves in time, and the streamfunction of the eigenvector of the instantaneous linear operator at that time.

the maximum eigenvalue of the instantaneous linear operator becomes positive. Second, when the maximum eigenvalue peaks, the shape of the optimal perturbation and the instantaneous eigenvector closely resemble one another. Third, when the maximum eigenvalue drops below zero, the energy of the optimal perturbation begins to decrease.

Due to this close relationship between the optimal perturbation and the quasi-steady state approximation, we now consider the influence of perturbing the flow with the instantaneous eigenvectors. At the initial perturbation time $t = 20$, the optimal perturbation and the instantaneous eigenvector are much different. In particular, the instantaneous eigenvector exhibits a much lower streamwise wavenumber, resulting in a larger structure. When we perturb with this eigenvector G_{v20}, we see minimal growth. At the peak of the maximum eigenvalue, the optimal perturbation and the instantaneous eigenvector closely match one another. However, if we perturb with the eigenvector at the peak G_{v45}, it results in orders of magnitude less growth. Also, if we perturb with this eigenvector at $t = 20$, it too results in far less growth. Although the instantaneous stability of the flow plays an important role in the evolution of the optimal perturbation, the instantaneous eigenvectors do not sufficiently align with the optimal perturbation needed to experience the maximum growth in energy. The optimal perturbation exhibits larger energy than the instantaneous eigenvectors because it can exhibit significant levels of transient growth before matching the shape of the eigenvector at the peak of the maximum eigenvalue. Past this point, the shape of the eigenvector remains nearly constant, so the optimal perturbation too maintains this shape. This also indicates that the quasi-steady state approximation is reasonable over this time interval, as the eigenvector does not change substantially. Lastly, we show the energy of the eigenvector once the eigenvalue becomes negative G_{v130}, which experiences minimal growth, as expected.

In figure 28 we show the same results as in figure 27 for PDF at $Re = 500$ and $\kappa = 0.1$. The optimal perturbation timing occurs when the maximum eigenvalue turns positive. The optimal perturbation starts with streamlines that are much more anti-aligned with the flow than the instantaneous eigenvector at this time. Then, the optimal perturbation grows and aligns with the instantaneous eigenvector at the peak of the maximum eigenvalue. This growth continues until the maximum eigenvalue drops below zero. As with WDF, the initial growth of the optimal perturbation plays an important role that is missed when
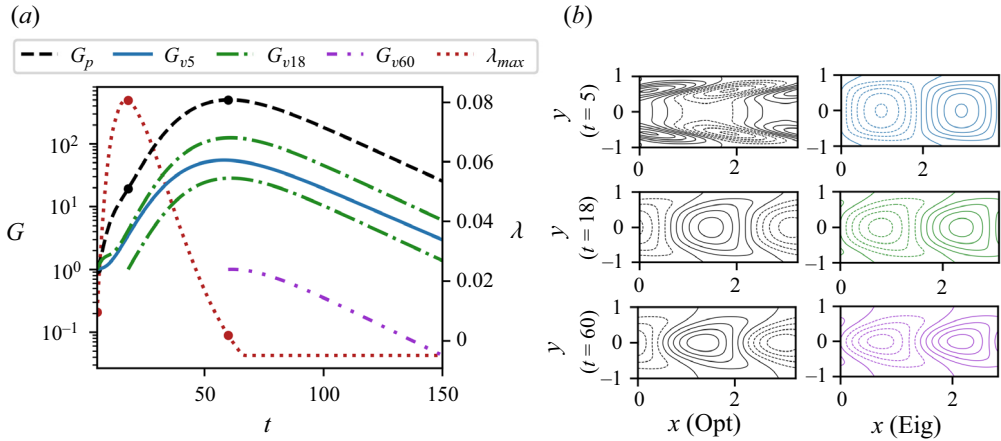
Figure 28. (*a*) Evolution of the optimal perturbation and of eigenvectors of the instantaneous linear operator for decelerating PDF ($Re = 500$, $\kappa = 0.1$) determined by the linearized equations of motion and the largest eigenvalue of the instantaneous linear operator. (*b*) Streamfunction of the perturbation as it evolves in time, and the streamfunction of the eigenvector of the instantaneous linear operator at that time.

only considering the instantaneous eigenvectors. In both WDF and PDF, as *Re* increases (at a sufficiently high κ), the peak of the maximum eigenvalue increases to larger times, thus leading to longer times over which this initial growth increases the energy of the perturbation.

Finally, we end by showing that G_{max,t_0} can be accurately approximated by integrating the instantaneous eigenvalue curve. Morón *et al.* (2022) showed for pulsatile flows with specific waveforms that G_{max,t_0} can be well approximated by

$$G_{LSA} = \mathrm{e}^{2\lambda_i},\tag{3.28}$$

where

$$\lambda_i = \int_{t_0}^{t_0 + \Delta t_u} \lambda_{max}(t)\,\mathrm{d}t.\tag{3.29}$$

Here, Δt_u stands for the time window where $\lambda_{max} > 0$. Note that Morón *et al.* (2022) include a time period T that cancels out; this is not relevant to our case as our flow is not pulsatile. In figure 29 we show how G_{max,t_0} and G_{LSA} change as we increase *Re* at $\kappa = 0.1$. Similar to $t_0 = 0$ (figure 10), the scaling of G_{max,t_0} changes from Re^2 to 10^{Re} as *Re* increases. For WDF, this transition occurs at $Re \approx 250$, which is far lower than the $t_0 = 0$ case, where it takes place at $Re \approx 400$. For PDF, transition arises near the same point, because the optimal perturbation timing is closer to zero. Additionally, figure 29 shows that G_{LSA} is a good proxy for the optimal energy growth. It shows the correct scaling at high *Re*, even though it slightly underestimates the growth.

4. Conclusions

We undertook a systematic investigation of the stability of unsteady accelerating and decelerating flows. An exact analytical solution for laminar flows with arbitrary wall motion and pressure gradients in channels has been derived, from which we selected a specific exponentially decaying profile for wall motion and flow rate that isolated the effects of acceleration and deceleration. With these analytical profiles, we investigated the
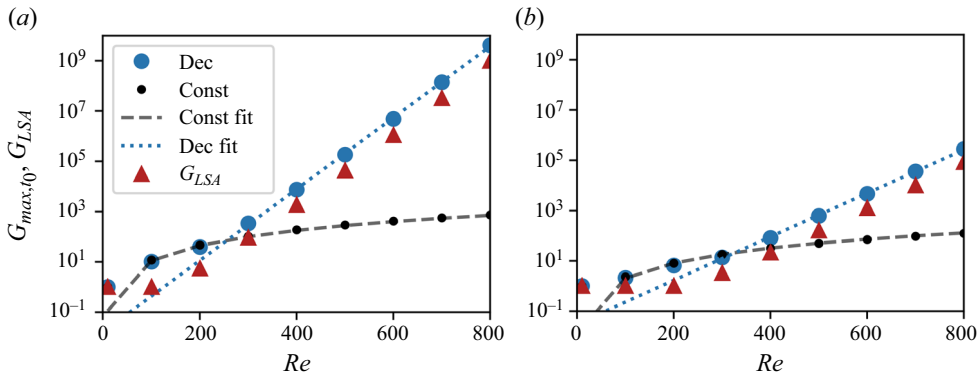
Figure 29. Plots of G_{max,t_0} and G_{LSA} as a function of Re for a decelerating flow at fixed $\kappa = 0.1$ ('Dec') and G_{max,t_0} for constant flow ('Const') for (*a*) WDF and (*b*) PDF. The fitting lines are described in the text.

stability of the flow with respect to these base flows through the linearized equations of motion by computing optimal perturbations. This investigation showed that deceleration can cause perturbations to exhibit massive amplification, while perturbations in the accelerating case never exceeded the maximum amplification of perturbations for a constant profile. Furthermore, the maximum amplification seen in the decelerating case exhibits both the Re^2 scaling seen in the constant case at low Re, and the 10^{Re} scaling seen in some unsteady cases at high Re.

This change in scaling arises due to a branch switching of the dominant perturbation in the decelerating case. At low Re and κ, we found that spanwise perturbations are most amplified, but upon increasing these values streamwise perturbations became most amplified. This was not the case for accelerating flows where spanwise perturbations always showed the largest amplification. We then studied the evolution of the optimal perturbations in time. In the case of acceleration, we found that the optimal perturbations stayed as streamwise vortices through time, similar to what was observed by Butler & Farrell ([1993](#)). However, in the case of deceleration, the perturbations grew due to the Orr mechanism, or the down-gradient Reynolds stress mechanism (Butler & Farrell [1993](#)). When streamlines are aligned with the laminar shear, there is growth. In the case of deceleration, the flow stops advecting the streamlines causing them to align opposite to the laminar shear of the base flow for extended periods of time, leading to growth. This behaviour does not happen in constant or accelerating flows since the laminar profile eventually aligns the streamlines with the laminar shear of the base flow. Furthermore, we found that this large growth of perturbations appears in DNS, both when the perturbation is applied directly or when random noise is imposed. Finally, we discovered that the optimal timing, when the perturbation is applied, is given by the instant when the maximum real eigenvalue of the instantaneous linear operator becomes positive.

In the future we intend to further explore how much the flow needs to decelerate for perturbations to exhibit the massive amplification shown here by using other temporal functions for the wall motion and flow rate. Additionally, these results could be extended to inform control strategies to avoid laminar transition. In the case of decelerating flows, this would require breaking up the formation of streamwise perturbations, and, in the case of acceleration, this would require breaking up spanwise perturbations. The fundamental insights from this study could also have implications for understanding the emergence of instabilities around accelerating and decelerating bodies of more complex geometries.
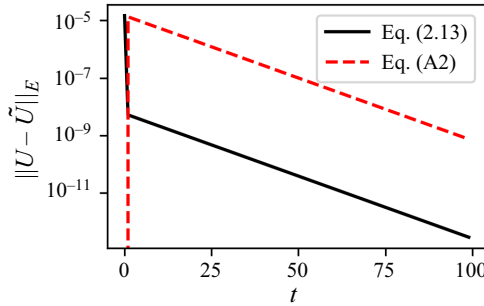
Figure 30. Error in the laminar profile for $K = 100$ modes using different forms of the laminar solution.

In particular, it may be the case that the destabilization around decelerating bodies could also be due to extended growth via the Orr mechanism.

Declaration of interests. The authors report no conflict of interest.

Author ORCIDs.

Alec J. Linot https://orcid.org/0000-0002-4591-7133;

Peter J. Schmid https://orcid.org/0000-0002-2257-8490;

Kunihiko Taira https://orcid.org/0000-0002-3762-8075.

Appendix A. Additional discussion on laminar flow solutions

We further discuss the choice of functions in (2.6), validate the laminar solutions against other analytical solutions for specific flows and provide a list of solutions for a family of unsteady flows. As mentioned in § 2, we could seek solutions in the wall-motion case of the form

$$U(y, t) = f_w(y, t) + g_w(t)y. \qquad (A1)$$

Following the procedure from § 2, this results in the laminar solution

$$U(y, t) = \sum_{n=1}^{\infty} e^{-a_n t} \left(\frac{2(-1)^n}{\pi n} \int_0^t e^{a_n t'} \frac{dg_w(t')}{dt} \, dt' + C_n \right) \sin(n\pi y) + g_w(t)y. \qquad (A2)$$

Although this equation has fewer terms than (2.14), the error is larger since it requires approximating y in terms of $\sin(n\pi y)$. In figure 30 we show the error between U approximated with $K = 10^5$ using (A2) (U) and $K = 100$ modes using both (2.14) and (A2) ($\tilde{U}$) for decelerating WDF ($Re = 500$ and $\kappa = 0.1$). In the $K = 10^5$ case, there is no discernible error between the two solutions. Figure 30 shows that a judicious choice of the form of (2.14) results in multiple orders of magnitude higher accuracy than the solution in (A2). The one exception to this is at $t = 0$ where there is a discontinuity in dg_c/dt, when evolving from constant simple shear, that does not change the results in (A2).

Next, we validate the laminar solution with three canonical problems: Stokes' first problem ($g_w = H(t)$), Stokes' second problem ($g_w = \sin(2\pi t)$) and Womersley flow ($g_p = -(2/Re)\sin(2\pi t)$) (Batchelor 2000; Majdalani 2008). In figure 31 we compare the solutions (A2), (2.14) and (2.25) against these three canonical problems at $Re = 10$.
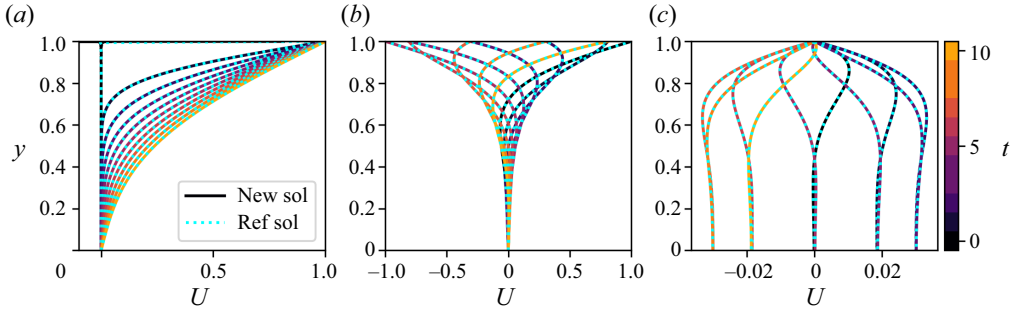
Figure 31. Laminar solutions using reference equations and the equations presented here for (*a*) Stokes' first problem, (*b*) Stokes' second problem and (*c*) Womersley flow.

Flow	Equation	Integral
$g_w(t) = H(t)$	(A2)	1
$g_w(t) = \sum_{m=-\infty}^{\infty} \hat{g}_m\, e^{i\omega_m t}$	(2.14)	$\sum_{m=-\infty}^{\infty} \frac{-\omega_m^2 \hat{g}_m}{a_n + i\omega_m}(e^{(a_n + i\omega_m)t} - 1)$
$g_w(t) = t^m$	(2.14)	$\frac{-m(m-1)a_n t^m}{(-a_n t)^m}(\Gamma(m-1) - \Gamma(m-1, -a_n t))$
$g_w(t) = \sum_{m=0}^{\infty} \hat{g}_m L_m^{(0)}(t)$	(2.14)	$\sum_{m=2}^{\infty} \sum_{l=0}^{\infty} \frac{(-1)^l \hat{g}_m}{a_n^{l+1}}(e^{a_n t} L_{m-2-l}^{(2+l)}(t) - L_{m-2-l}^{(2+l)}(0))$
$g_w(t) = u_i e^{-\kappa t} + u_f(1 - e^{-\kappa t})$	(2.14)	$\frac{\kappa^2(u_i - u_f)}{a_n - \kappa}(e^{(a_n - \kappa)t} - 1)$
$g_p(t) = \sum_{m=-\infty}^{\infty} \hat{g}_m\, e^{i\omega_m t}$	(2.25)	$\sum_{m=-\infty}^{\infty} \frac{i\omega_m \hat{g}_m}{b_n + i\omega_m}(e^{(b_n + i\omega_m)t} - 1)$

Table 1. Integral expressions in the laminar solutions for specific flows.

Notably, we present both Stokes' second problem and the Womersley flow after the transient from the initial condition has approached zero.

We summarize in table 1 the integrals in (A2), (2.14) and (2.25) for some interesting boundary conditions, and for generic Womersley flow. The cases that we include are Stokes' first problem, a generalization of Stokes' second problem for all periodic functions, the polynomial t^m, Laguerre polynomials ($L_m^{(\alpha)}(t)$), which is the natural basis for polynomial functions with $t \in [0, \infty]$, the exponential decaying flow considered above and a generalization of Womersley flow for all periodic functions. Note that, in the polynomial cases, we are assuming that the polynomial is twice differentiable. For t^m, this implies $m \in \mathbb{Z}^+$ and $m > 1$. Also, Γ represents the ordinary gamma function, if it takes one argument, and the incomplete gamma function, if it takes two input values.

Appendix B. Converting the energy norm to the L_2-norm

Here we outline the procedure for converting the energy norm to the L_2 norm. This procedure depends upon how we discretize $\mathcal{L}$. Specifically, in (3.11) we must approximate the two derivative operators D^2 and D^4. Early approaches (Farrell 1988) used finite-difference methods for approximating these derivatives, but we instead choose Chebyshev differentiation matrices (Reddy & Henningson 1993; Weideman & Reddy 2000) to approximate derivatives. Spectral methods exhibit superior convergence, which reduces the number of collocation points required for our computations. Additionally, Chebyshev collocation points (also known as Gauss–Lobatto points Peyret 2002) are well

suited for our flows of interest since they are more densely clustered near the walls of the domain where we exhibit larger gradients. However, defining q on these collocation points necessitates accounting for the non-uniform grid when evaluating (3.20).

To address this non-uniform spacing, consider the inner product

$$\langle \hat{\omega}_y, \hat{\omega}_y \rangle_L = \int_{-1}^{1} \hat{\omega}_y^* \hat{\omega}_y \, \mathrm{d}y \approx \sum_{i=1}^{M-1} \hat{\omega}_y(y_i)^* \hat{\omega}_y(y_i) \Delta y_i, \tag{B1}$$

where

$$y_i = \cos\left(\frac{\pi i}{M}\right), \quad i = 0, \dots, M, \tag{B2}$$

with M grid points. With this definition, we can construct a diagonal weight matrix W to account for Δy_i and transform the inner product on a non-uniform grid into a standard L_2 norm with

$$\langle \hat{\omega}_y, \hat{\omega}_y \rangle_L \approx \| W^{1/2} \hat{\omega}_y \|^2. \tag{B3}$$

While this allows us to convert all terms in the integral in (3.20) to standard L_2 norms we are still left with the presence of derivates of q in the energy norm.

To proceed, we must convert (3.20) to one inner product in terms of $\hat{v}$ and one in terms of $\hat{\omega}_y$. For this reason, we consider the inner product

$$\langle (D + \sqrt{k^2}) \hat{v}, (D + \sqrt{k^2}) \hat{v} \rangle_L$$
$$= \langle D\hat{v}, D\hat{v} \rangle_L + \langle \sqrt{k^2} \hat{v}, \sqrt{k^2} \hat{v} \rangle_L + \langle D\hat{v}, \sqrt{k^2} \hat{v} \rangle_L + \langle \sqrt{k^2} \hat{v}, D\hat{v} \rangle_L. \tag{B4}$$

The right-hand-side of (B4) includes the two terms in (3.20), with two additional cross-terms. We can evaluate these cross-terms by rewriting the above equations in integral form:

$$\langle D\hat{v}, \sqrt{k^2} \hat{v} \rangle_L + \langle \sqrt{k^2} \hat{v}, D\hat{v} \rangle_L = \int_{-1}^{1} \frac{\partial \hat{v}^*}{\partial y} \sqrt{k^2} \hat{v} \, \mathrm{d}y + \int_{-1}^{1} \sqrt{k^2} \hat{v}^* \frac{\partial \hat{v}}{\partial y} \, \mathrm{d}y. \tag{B5}$$

Integrating by parts, which we demonstrate on the second integral, we see that the resulting terms sum to zero:

$$\langle D\hat{v}, \sqrt{k^2} \hat{v} \rangle_L + \langle \sqrt{k^2} \hat{v}, D\hat{v} \rangle_L$$
$$= \int_{-1}^{1} \frac{\partial \hat{v}^*}{\partial y} \sqrt{k^2} \hat{v} \, \mathrm{d}y + \sqrt{k^2} \hat{v}^* \hat{v}|_{-1}^{1} - \int_{-1}^{1} \sqrt{k^2} \hat{v} \frac{\partial \hat{v}^*}{\partial y} \, \mathrm{d}y = 0. \tag{B6}$$

This allows us to rewrite (3.20) as

$$\|q\|_E^2 = \langle (D + \sqrt{k^2}) \hat{v}, (D + \sqrt{k^2}) \hat{v} \rangle_L + \langle \hat{\omega}_y, \hat{\omega}_y \rangle_L, \tag{B7}$$

which we combine with (B3) to convert the energy norm into the L_2 norm

$$\|q\|_E^2 = \left\| \begin{bmatrix} W^{1/2}(D + \sqrt{k^2}) & 0 \\ 0 & W^{1/2} \end{bmatrix} q \right\|^2 = \|Vq\|^2. \tag{B8}$$

We use V to in 3.21 to compute the maximum amplification.
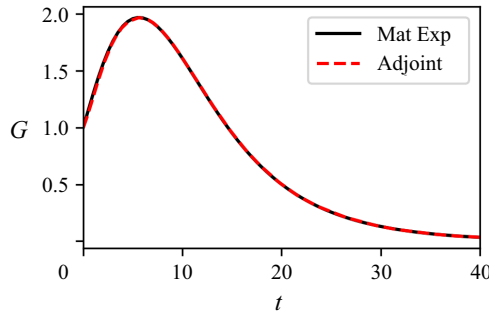
999 A43-38

Figure 32. Maximum amplification of energy density G using the adjoint method and the matrix exponential method.

Appendix C. Computation of non-normal growth

We compare our use of the matrix exponential method for computing the energy amplification to the adjoint method for computing non-normal growth. For this comparison, we use the laminar PDF that is impulsively stopped to a zero flow rate given in Nayak & Das (2017). Figure 32 shows the growth for perturbations of the laminar base flow using both the matrix exponential method ((3.21)) and the adjoint method (Nayak & Das 2017). The two curves are in excellent agreement suggesting both choices give equivalent solutions. The matrix exponential method has the advantage that only matrix multiplications for the forward solution are needed, while the adjoint method requires solving a forward problem and a backward problem iteratively. For the channel flow cases we considered in this work, the linearized equations of motion result in a small matrix, however, this method would not be feasible when a larger matrix is required, in which case the adjoint method would be preferable.

Appendix D. Solving for the pressure gradient when given a flow rate

Here, we introduce a method for numerically approximating the pressure gradient g_p for a prescribed flow rate assuming no even wall motion (i.e. $g_e(t) = 0$). Even though we could numerically approximate both the integral and the time derivative in (2.28), we instead perform integration by parts to eliminate the time derivative in (2.28), which leaves us with an approximation of the integral only. Using integration by parts we obtain the following equation:

$$
\mathrm{e}^{-b_n t} \int_0^t \mathrm{e}^{b_n t'} \frac{\mathrm{d} g_p}{\mathrm{d} t}\, \mathrm{d} t' = \hat{g}_p(t) - \mathrm{e}^{-b_n t}\hat{g}_p(0) + \mathrm{e}^{-b_n t} H(t)\hat{g}_0 - b_n\, \mathrm{e}^{-b_n t} \int_0^t \mathrm{e}^{b_n t'} \hat{g}_p\, \mathrm{d} t'.
$$

$$(D1)$$

Combining (2.28) with (D1), we find that

$$
Q(t) = \sum_{n=0}^{\infty} \frac{32\, \mathrm{e}^{-b_n t} Re}{(2\pi n + \pi)^4} \left(H(t)\hat{g}_0 - \hat{g}_p(0) - b_n \int_0^t \mathrm{e}^{b_n t'} \hat{g}_p(t')\, \mathrm{d} t' \right) + \frac{2(-1)^n\, \mathrm{e}^{-b_n t} C_{2,n}}{2\pi n + \pi}.
$$

$$(D2)$$

999 A43-39

Using the trapezoidal rule to approximate the integral in (D2) we arrive at an expression for the temporal evolution of the pressure gradient:

$$\hat{g}_p(l\Delta t) \sum_{n=0}^{\infty} d_n \approx \hat{g}_p((l-1)\Delta t) \sum_{n=0}^{\infty} d_n \, \mathrm{e}^{-b_n \Delta t}$$

$$- \sum_{n=0}^{\infty} \sum_{j=1}^{l-1} d_n (\mathrm{e}^{-b_n(l-j)\Delta t} \hat{g}_p(j\Delta t) + \mathrm{e}^{-b_n(l-(j-1))\Delta t} \hat{g}_p((j-1)\Delta t) + R(l\Delta t). \quad \text{(D3)}$$

Here $d_n = 4\Delta t/(2\pi n + \pi)^2$ and

$$R(t) = -Q(t) + \sum_{n=0}^{\infty} \frac{32\,\mathrm{e}^{-b_n t} Re}{(2\pi n + \pi)^4}(H(t)\hat{g}_0 - \hat{g}_p(0)) + \frac{2(-1)^n \,\mathrm{e}^{-b_n t} C_{2,n}}{2\pi n + \pi}. \quad \text{(D4)}$$

Note that the factor of 2 from the trapezoidal rule has been incorporated into d_n. Finally, we can compute the velocity profile corresponding to this pressure gradient by again using integration by parts ((D1)) to simplify (2.17) and by approximating the resulting integral with the trapezoidal rule leading to

$$U(y, l\Delta t) \approx - \sum_{n=0}^{\infty} \sum_{j=1}^{l} \left\{ \frac{d_n(-1)^n}{2}[\mathrm{e}^{-b_n(l-j)\Delta t}\hat{g}_p(j\Delta t) + \mathrm{e}^{-b_n(l-(j-1))\Delta t}\hat{g}_p((j-1)\Delta t)] \right\}$$

$$\cos\left[\left(n + \frac{1}{2}\right)\pi y\right] + \sum_{n=0}^{\infty} \mathrm{e}^{-b_n l\Delta t} \left[\frac{16(-1)^n Re}{(2\pi n + \pi)^3}(H(l\Delta t)\hat{g}_0 - \hat{g}_p(0)) + C_{2,n} \right]$$

$$\cos\left[\left(n + \frac{1}{2}\right)\pi y\right]. \quad \text{(D5)}$$

REFERENCES

ANDERSSON, P., BERGGREN, M. & HENNINGSON, D.S. 1999 Optimal disturbances and bypass transition in boundary layers. *Phys. Fluids* **11** (1), 134–150.

BATCHELOR, G.K. 2000 *An Introduction to Fluid Dynamics*, Cambridge Mathematical Library. Cambridge University Press.

BIAU, D. 2016 Transient growth of perturbations in Stokes oscillatory flows. *J. Fluid Mech.* **794**, R4.

BIRD, R.B., STEWART, W.E., LIGHTFOOT, E.N. & KLINGENBERG, D.J. 2015 *Introductory Transport Phenomena*. Wiley Publishing.

BUTLER, K.M. & FARRELL, B.F. 1992 Three-dimensional optimal perturbations in viscous shear flow. *Phys. Fluids* A **4** (8), 1637–1650.

BUTLER, K.M. & FARRELL, B.F. 1993 Optimal perturbations and streak spacing in wall-bounded turbulent shear flow. *Phys. Fluids* A **5** (3), 774–777.

CONRAD, P.W. & CRIMINALE, W.O. 1965 The stability of time-dependent laminar flow: parallel flows. *Z. Angew. Math. Phys.* **16** (2), 233–254.

DAIDZIC, N.E. 2022 Unified theory of unsteady planar laminar flow in the presence of arbitrary pressure gradients and boundary movement. *Symmetry* **14** (4), 757.

DAVIS, S.H. 1976 The stability of time-periodic flows. *Annu. Rev. Fluid Mech.* **8** (1), 57–74.

DEEN, W.M. 2012 *Analysis of Transport Phenomena*. Oxford University Press.

DRAZIN, P.G. & RILEY, N. 2006 *The Navier–Stokes Equations: A Classification of Flows and Exact Solutions*. Cambridge University Press.

FAN, C. 1964 Non-steady, viscous, incompressible flow in cylindrical and rectangular conduits (with emphasis on periodically oscillating flow). PhD thesis, ProQuest Dissertations & Theses.

FARRELL, B.F. 1988 Optimal excitation of perturbations in viscous shear flow. *Phys. Fluids* **31** (8), 2093–2102.

GERRARD, J.H. 1971 An experimental investigation of pulsating turbulent water flow in a tube. *J. Fluid Mech.* **46**, 43–64.

GIBSON, J.F. 2012 Channelflow: a spectral Navier–Stokes simulator in C++. *Univ. New Hampshire*, 1–41.

GIBSON, J.F., *et al.* 2021 Channelflow 2.0. arXiv:channelflow.ch.

GRAHAM, M.D. & RAWLINGS, J.B. 2013 *Modeling and Analysis Principles for Chemical and Biological Engineers*. Nob Hill Publishing.

GREENBLATT, D. & MOSS, E.A. 2004 Rapid temporal acceleration of a turbulent pipe flow. *J. Fluid Mech.* **514**, 65–75.

GUAZZELLI, E. & HINCH, J. 2011 Fluctuations and instability in sedimentation. *Annu. Rev. Fluid Mech.* **43** (1), 97–116.

GUSTAVSSON, L.H. 1986 Excitation of direct resonances in plane Poiseuille flow. *Stud. Appl. Maths* **75** (3), 227–248.

HE, S. & JACKSON, J.D. 2000 A study of turbulence under conditions of transient flow in a pipe. *J. Fluid Mech.* **408**, 1–38.

HINO, M., KASHIWAYANAGI, M., NAKAYAMA, A. & HARA, T. 1983 Experiments on the turbulence statistics and the structure of a reciprocating oscillatory flow. *J. Fluid Mech.* **131**, 363–400.

ITO, H. 1952 Theory of laminar flow through a pipe with non-steady pressure gradients. *Trans. Japan Soc. Mech. Engng* **18** (66), 101–108.

JONES, A.R. 2020 Gust encounters of rigid wings: taming the parameter space. *Phys. Rev. Fluids* **5**, 110513.

JOSEPH, D.D. 1976 *Stability of Fluid Motions I*. Springer.

KANNAIYAN, A., NATARAJAN, S. & VINOTH, B.R. 2022 Stability of a laminar pipe flow subjected to a step-like increase in the flow rate. *Phys. Fluids* **34** (6), 064102.

KANNAIYAN, A., VARATHALINGARAJAH, T. & NATARAJAN, S. 2021 Analytical solutions for the incompressible laminar pipe flow rapidly subjected to the arbitrary change in the flow rate. *Phys. Fluids* **33** (4), 043601.

KATAOKA, K., KAWABATA, T. & MIKI, K. 1975 The start-up response of pipe flow to a step change in flow rate. *J. Chem. Engng Japan* **8** (4), 266–271.

VON KERCZEK, C.H. 1982 The instability of oscillatory plane Poiseuille flow. *J. Fluid Mech.* **116**, 91–114.

VON KERCZEK, C.H. & DAVIS, S.H. 1974 Linear stability theory of oscillatory Stokes layers. *J. Fluid Mech.* **62** (4), 753–773.

KUROKAWA, J. & MORIKAWA, M. 1986 Accelerated and decelerated flows in a circular pipe: 1st report, velocity profile and friction coefficient. *Bull. JSME* **29** (249), 758–765.

LEE, Y. 2017 Analytical solutions of channel and duct flows due to general pressure gradients. *Appl. Math. Model.* **43**, 279–286.

LINOT, A.J., ZENG, K. & GRAHAM, M.D. 2023*a* PyChannel. https://github.com/alinot5/PyChannel.

LINOT, A.J., ZENG, K. & GRAHAM, M.D. 2023*b* Turbulence control in plane Couette flow using low-dimensional neural ODE-based models and deep reinforcement learning. *Intl J. Heat Fluid Flow* **101**, 109139.

LIU, C.-M. 2008 Complete solutions to extended Stokes' problems. *Math. Prob. Engng* **2008**, 754262.

MAJDALANI, J. 2008 Exact Navier–Stokes solution for the pulsatory viscous channel flow with arbitrary pressure gradient. *J. Propul. Power* **24** (6), 1412–1423.

MCCROSKEY, W.J. 1981 The phenomenon of dynamic stall. *NASA TM* 81264.

MORÓN, D. & AVILA, M. 2024 Turbulent puffs in transitional pulsatile pipe flow at moderate pulsation amplitudes. *Phys. Rev. Fluids* **9**, 024601.

MORÓN, D., FELDMANN, D. & AVILA, M. 2022 Effect of waveform on turbulence transition in pulsatile pipe flow. *J. Fluid Mech.* **948**, A20.

NAYAK, A. & DAS, D. 2017 Transient growth of optimal perturbation in a decaying channel flow. *Phys. Fluids* **29** (6), 064104.

PEYRET, R. 2002 *Spectral Methods for Incompressible Viscous Flow*, Applied Mathematical Sciences. Springer.

PIER, B. & SCHMID, P.J. 2017 Linear and nonlinear dynamics of pulsatile channel flow. *J. Fluid Mech.* **815**, 435–480.

REDDY, S.C. & HENNINGSON, D.S. 1993 Energy growth in viscous channel flows. *J. Fluid Mech.* **252**, 209–238.

SCHLICHTING, H. & GERSTEN, K. 2017 *Boundary-Layer Theory*, 9th edn. Springer.

SCHMID, P.J. & HENNINGSON, D.S. 1994 Optimal energy density growth in Hagen–Poiseuille flow. *J. Fluid Mech.* **277**, 197–225.

SCHMID, P.J. & HENNINGSON, D.S. 2001 *Stability and Transition in Shear Flows*. Springer.

SEBORG, D.E., MELLICHAMP, D.A., EDGAR, T.F. & DOYLE, F.J. 2010 *Process Dynamics and Control*. John Wiley & Sons.

SENGUPTA, T.K., LIM, T.T., SAJJAN, S.V., GANESH, S. & SORIA, J. 2007 Accelerated flow past a symmetric aerofoil: experiments and computations. *J. Fluid Mech.* **591**, 255–288.

SERRIN, J. 1959 On the stability of viscous fluid motions. *Arch. Rat. Mech. Anal.* **3** (1), 1–13.

SHEN, S.F. 1961 Some considerations on the laminar stability of time-dependent basic flows. *J. Aerosp. Sci.* **28** (5), 397–404.

SHUY, E.B. 1996 Wall shear stress in accelerating and decelerating turbulent pipe flows. *J. Hydraul. Res.* **34** (2), 173–183.

SPALART, P.R., MOSER, R.D. & ROGERS, M.M. 1991 Spectral methods for the Navier–Stokes equations with one infinite and two periodic directions. *J. Comput. Phys.* **96** (2), 297–324.

SZYMANSKI, G. 1932 Quelques solutions exactes des équations d'hydrodynamique du fluide visqueux dans le cas d'un tube cylindrique. *J. Math. Pures Appl.* **11**, 67–108.

TOZZI, J.T. & VON KERCZEK, C.H. 1986 The stability of oscillatory Hagen-Poiseuille flow. *J. Appl. Mech.* **53** (1), 187–192.

TREFETHEN, L.N., TREFETHEN, A.E., REDDY, S.C. & DRISCOLL, T.A. 1993 Hydrodynamic stability without eigenvalues. *Science* **261** (5121), 578–584.

URBANOWICZ, K., BERGANT, A., STOSIAK, M., DEPTUŁA, A. & KARPENKO, M. 2023 Navier–Stokes solutions for accelerating pipe flow – a review of analytical models. *Energies* **16** (3), 1407.

WEIDEMAN, J.A. & REDDY, S.C. 2000 A MATLAB differentiation matrix suite. *ACM Trans. Math. Softw.* **26** (4), 465–519.

WOMERSLEY, J.R. 1955 Method for the calculation of velocity, rate of flow and viscous drag in arteries when the pressure gradient is known. *J. Physiol.* **127** (3), 553–563.

XU, D., SONG, B. & AVILA, M. 2021 Non-modal transient growth of disturbances in pulsatile and oscillatory pipe flows. *J. Fluid Mech.* **907**, R5.